Final Report
Department of Homeland Security

Advanced Detection and Mitigation of Wind Turbine Clutter for the Multi-Mission Phased Array Radar (MPAR) Program

Robert D. Palmer and Sebastián Torres

Graduate Research Assistant: Feng Nai

Atmospheric Radar Research Center
University of Oklahoma
September 2011

Chapter 1

Introduction and Motivation

1.1 Wind Energy Growth

Wind energy is growing rapidly in the United States. From 2006 to 2009, wind energy consumption increased from 264 MBtu to 924 MBtu. In 2009 alone, the capacity for wind generated electricity increased 3.6 GW (Energy Information Administration 2011). Typical wind turbine consists of three major components: the tower, the nacelle, and the blades. Figure 1.1 shows such a wind turbine in a wind farm. After the initial cost to install the wind turbines and the necessary transmission infrastructure, only routine maintenance is required throughout the lifetime of a turbine. This reduces the long-term cost of wind energy. Considering the uncertain supply and the increasing price of fossil fuels, wind energy is being pushed as a premier source of clean energy for the future. A report published by the Department of Energy in 2008 detailed a scenario where 20% of the Nation's energy will be generated through wind power by 2030 (Department of Energy 2008). The projected growth of wind power required to achieve such scenario is shown in Figure 1.2. While there are many positive outcomes from the growth of wind energy, the negative effects of the expansion of wind farms cannot be ignored. One such negative impact is the interference caused by the wind turbines on radar systems, especially weather radars. Such interference is generally referred to as wind turbine clutter (WTC). As wind turbines grow in size and new wind farms are constructed, the interference problem is only going to get worse.

1.2 Effects of Wind Turbines on Radar

The United States has a network of weather radars that are constantly collecting information about the atmosphere. The radar transmit a pulse of electromagnetic energy and measures the energy reflected from the hydrometeors in the atmosphere. Based on the reflected energy, weather radar estimates three meteorological variables, also known as moments, that describes the conditions of the atmosphere. The three moments are called reflectivity, Doppler velocity, and spectrum width. Reflectivity is based on the strength of the reflected energy and it describes the general strength of a storm and measures the amount of hydrometeors present. Doppler velocity measure the mean motion of the hydrometeors in the radial direction relative to the radar. Spectrum width describes the turbulence of the hydrometeors inside the volume of space under observation, which is called resolution volume (Doviak and Zrnić 1993). Other advanced algorithms uses these moments as input to perform tasks such as estimate precipitation and detect severe weathers such as tornados.

Figure 1.1: Typical three-blade wind turbine consisting of a tower, nacelle, and three blades. The blades are constructed of composite materials with lightning cables spanning the length of each blade and the nacelle houses the generator and the equipment that controls the turbine

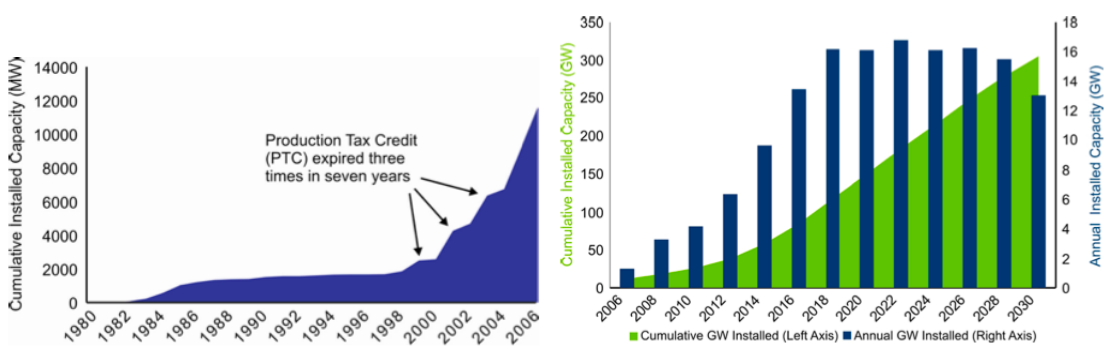

(a) Growth through 2006 (b) Required Growth

Figure 1.2: (a) Cumulative installed capacity of wind power in the United States. (b) Required growth to reach the goal of 20% wind power by 2030. (Department of Energy 2008)

When the weather radar is observing the atmosphere, the energy reflected from non-hydrometeors generate unwanted clutter signals. When a resolution volume contains both hydrometeors and clutter targets, the weather signal and the unwanted clutter signal are coherently added adversely affecting the three moments. The most common clutter signal is ground clutter, which is generated when energy is reflected from non-moving targets such as ground, buildings, and trees. Wind turbines with its moving blades generate a much more complex clutter signal.

It is well documented that wind farms cause problems for single target radar systems such as air traffic control radars (ATC). The ground clutter caused by the tower reduces the probability of detection for an ATC radar (Tietjen 2005) and the automatic tracking algorithms can miss a detection or generate false alarms on the location of an aircraft while it flies over a wind farm (Perry and Biss 2007). The problem for weather radar systems is more complicated.

The return signals from WTC are very similar to weather signals and are difficult to distinguish on a plan position indicator (PPI) plot. One example of such confusion is illustrated in Figure 1.3. Experience human operators can identify the presence of WTC, but it is much more difficult for automatic algorithms to identify such contamination. If not mitigated, WTC will bias the three moments and automatic algorithms such as quantitative precipitation estimation that uses these moments will be biases as well (Vogt et al. 2007). Tornado detection algorithms also have the potential to generate false detections and cause forecasting problems (Vogt et al. 2007). The traditional approach to mitigate the bias caused by clutter is to apply a frequency domain filter to remove the clutter signal before moment estimation. However, because the moving blades of the wind turbine, such approach is ineffective at removing WTC while preserving the weather signal simultaneously.

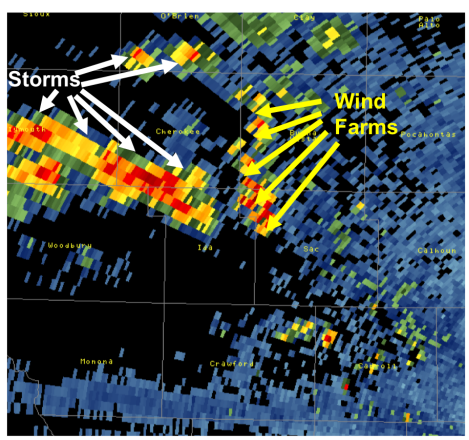

Figure 1.3: Similar radar returns of storms and WTC on a PPI plot. Image courtesy of the Radar Operation Center, Application Branch.

1.3 Motivation for Proposed Mitigation Algorithm

Since traditional filtering approaches are ineffective at mitigating WTC, a new algorithm needs to be developed before WTC becomes a wide spread problem for the national weather radar network. Detailed studies of WTC have been conducted to understand WTC signatures (Isom et al. 2009), but have focused on using a radar in a spotlight mode, where the beam is not rotated. Such modes are not operational.

This report outlines a unique algorithm based on mimicking human perception of spatial continuity in weather radar images. In other words, the proposed algorithm uses the inherent range continuity in the spectral characteristics of a weather field to assist in determining the spectral coefficients to use for moment estimation. By doing so, it will be shown that biases can be greatly reduced in both stratiform and convective precipitation. As important is the fact that the algorithm has the potential for realtime implementation given that the processing is conducted along each radial independently. Furthermore, application to phased array radar may even have more potential since no beam smearing effects are present with such systems.

Chapter 2

Range-Doppler Signal Processing

The range-Doppler spectrum shows key differences between weather signals and WTC signals. Two methods to exploit the spatial and spectral differences are presented in this chapter to mitigate WTC contamination. After a brief review of the definition of the range-Doppler spectrum, the advantages of using the range-Doppler spectrum to mitigate WTC are discussed. The first mitigation method is based on detecting the discontinuities, or image edges, in the range-Doppler spectrum caused by the WTC, while the second mitigation method is based on exploiting the continuity of weather signals.

2.1 Definition of Range-Doppler Spectrum

The range-Doppler spectrum, denoted by $S(v, r)$, is a plot of Doppler spectra for a set of contiguous range gates as a two-dimensional image, where the x-axis is Doppler velocity, the y-axis is range, and the color of each pixel represents the power in dB units at that frequency bin and range gate. The range-Doppler concept has been used in wind profiling communities (Wilfong et al. 1993; Merrit 1995) and the recently developed NIMA algorithm (Morse et al. 2002) also takes advantage of the range-Doppler spectrum to mitigate contamination for a wind profiling radar. In this work, the range gates in a range-Doppler spectrum are labeled by discrete indicies n rather than the range r. Since the actual distance between the range gates and the radar is not used by any of the algorithms in this chapter, the discrete indexing makes it more convenient to explain the algorithms. The discrete index is related to the range by

$$r(n) = n\Delta r + r_{min} \tag{2.1}$$

where $r(n)$ is the range of the nth gate, Δr is the range resolution of the radar, and r_{min} is the range of the first gate in the range-Doppler spectrum.

Examples of Range-Doppler spectra for stratiform precipitation, convective storm, and clear air conditions are shown next. In the stratiform precipitation case, the weather spectra from different range gates have similar power, velocity, and spectrum width. Figure 2.1 is a simulated stratiform precipitation range-Doppler spectrum based on data collected by WSR-88D KTLX, located in Oklahoma City, OK, on November 15, 2010. The simulation procedure is explained in Section 3.1.1. In this spectrum, the weather signal is present in each range gate shown and has velocities centered around 7 $\mathrm{m\,s^{-1}}$. In contrast to stratiform precipitation, convective storms can show much more variability in the spectral moments as a function of range. Figure 2.2 shows a simulated convective storm range-Doppler spectrum based on observations by KTLX on May 1, 2009. The power of the weather signal increases

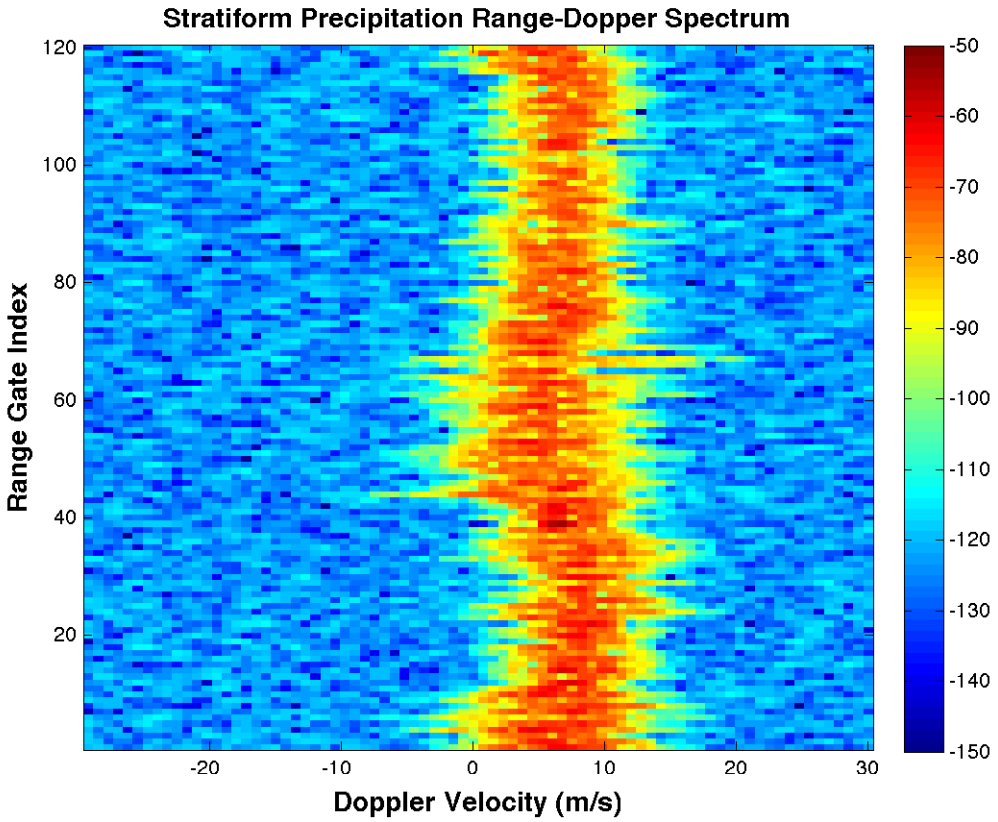

Figure 2.1: Range-Doppler spectrum of stratiform precipitation. There is little velocity shear in range. The signal power and spectrum width have little variation in range.

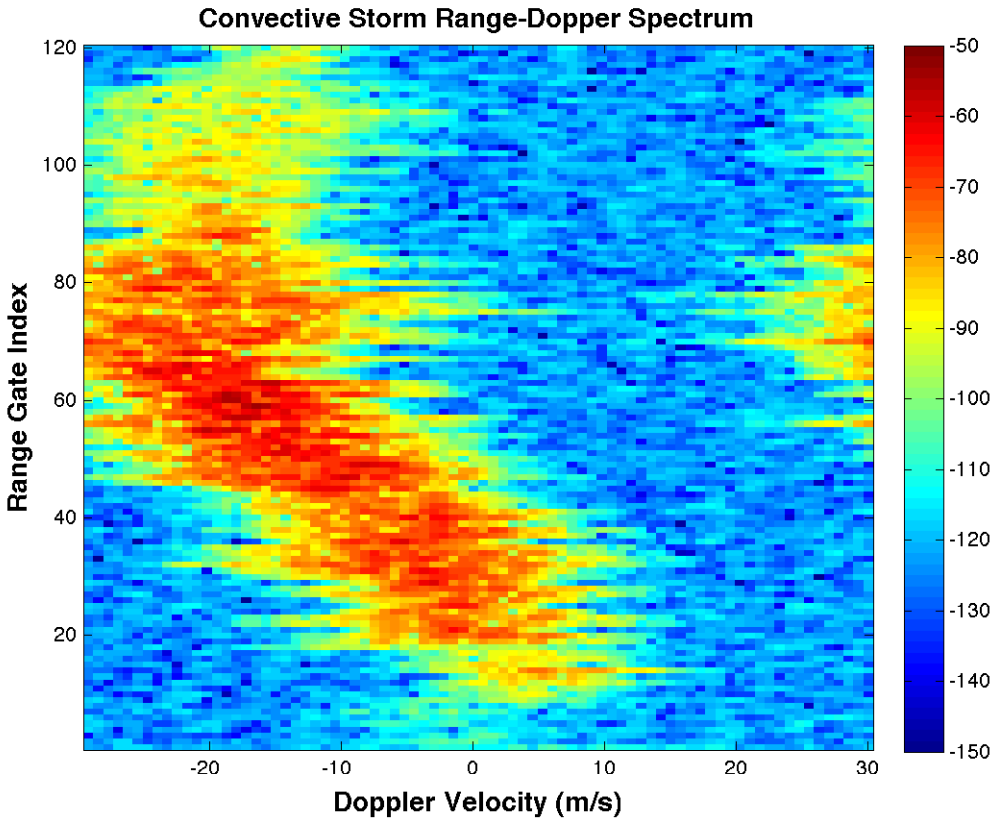

Figure 2.2: Range-Doppler spectrum of a convective storm. There is large velocity shear and signal power variation in range. The spectrum width has less variations in range.

between range gate 1 and 60 and then decreases; the velocity of the weather signal starts around zero and decreases linearly to around -20 $\mathrm{m\,s^{-1}}$. The spectrum width has slightly less variation than the other two moments, but there are large differences in spectrum width between range gates that are farther apart. For example, spectrum width estimate for gate 75 is larger than the spectrum width estimate for gate 45 by 4 $\mathrm{m\,s^{-1}}$. Aliasing occurs between gates 64 and 86. Figure 2.3 is a simulated clear

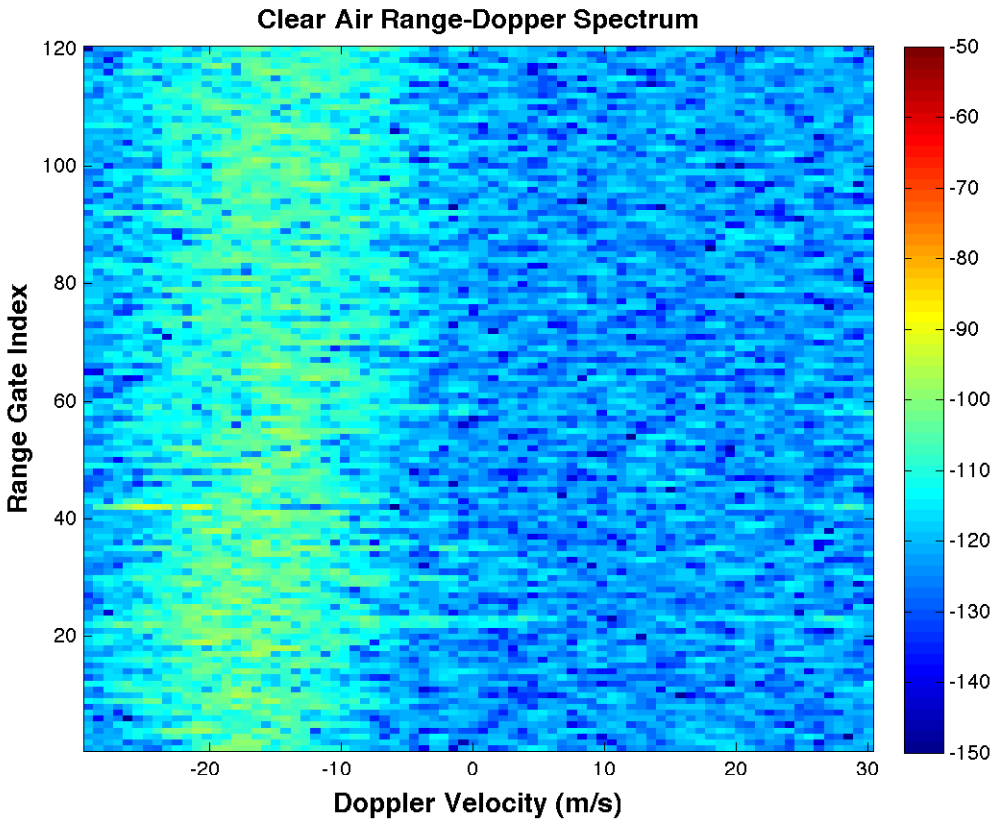

Figure 2.3: Range-Doppler spectrum of clear air. The return signal power is weak compared to the background noise power.

air range-Doppler spectrum based on observations by KTLX on November 15, 2010. The range-Doppler spectrum is similar to the stratiform spectrum shown in Figure 2.1 except the signal powers are significantly lower and the velocities are centered around -18 $\mathrm{m\,s^{-1}}$.

Observing the three examples of weather range-Doppler spectra, the common feature is that weather signals from one range gate are similar to weather signals in neighboring range gates. Both WTC mitigation methods proposed in this chapter use this key feature to help identify the spectrum of the weather signal in a contaminated gate.

2.2 Advantages of Range-Doppler Processing

There are several advantages of using the range-Doppler spectrum to mitigate WTC contamination. The first advantage is that the dwell time in operational radars is often long enough to collect signal samples required to estimate the range-Doppler spectrum with sufficient precision. In contrast, the gate-by-gate methods require much longer dwell times to collect enough samples to observe the non-stationary features of the WTC. Also, estimation of the range-Doppler spectrum only requires time-series data one dwell. Thus, an operational WTC mitigation algorithm based on the range-Doppler spectrum would function under current operational settings of the WSR-88D, while gate-by-gate methods would certainly require modifications to the operational scanning strategies.

The second advantage of using the range-Doppler spectrum is that the mitigation methods follow the steps a human expert would use to estimate the spectral moments for the contaminated range gates. Examining a range-Doppler spectrum with weather and WTC contamination, an expert can use the spectrum of neighboring non-contaminated gates to identify the spectral coefficients in the contaminated gates that might be related to the weather signal. Figure 2.4 shows a contaminated range-Doppler spectrum. Range gate 43 to 70 are contaminated, and it is difficult to locate the weather signal in the contaminated gates if no other information is available. However, by observing the trend in the weather signal in range gates 30 to 42 and 71 to 82, an expert can make an estimate of the frequency content of the weather signal in the contaminated gates. A possible estimated "weather window" is overlaid on the contaminated spectrum shown in Figure 2.4. The weather window, represented by the horizontal bars, indicates the spectral coefficients that are likely to contain most of the weather signal. Assuming the weather signal is continuous in range, since the weather window in the non-contaminated gates includes the majority of the significant spectral coefficients of the weather signal, it is likely that significant weather spectral coefficients in the contaminated gates are included in the weather window as well. Thus, the spectral moments of the weather signal in the contaminated gates can be estimated using only the spectral coefficients included in the weather window, which may significantly reduce the biases caused by the WTC.

2.3 The Edge Detection Method

The edge detection method (EDM) is the first approach that uses the range-Doppler spectrum to mitigate WTC contamination. It focuses on the sharp transitions in the range dimension of the range-Doppler spectrum caused by the WTC contamination. By modeling such transitions as step edges, a method is developed to detect and remove the frequency bins containing only WTC power. Since only the first range gate in a block of gates contaminated by WTC can create an edge, the method is used recursively to mitigate one contaminated gate at a time until all contaminated gates are processed.The theory and advantages of the edge detection method are discussed in Section 2.3.1, a detailed explanation of the steps in the edge

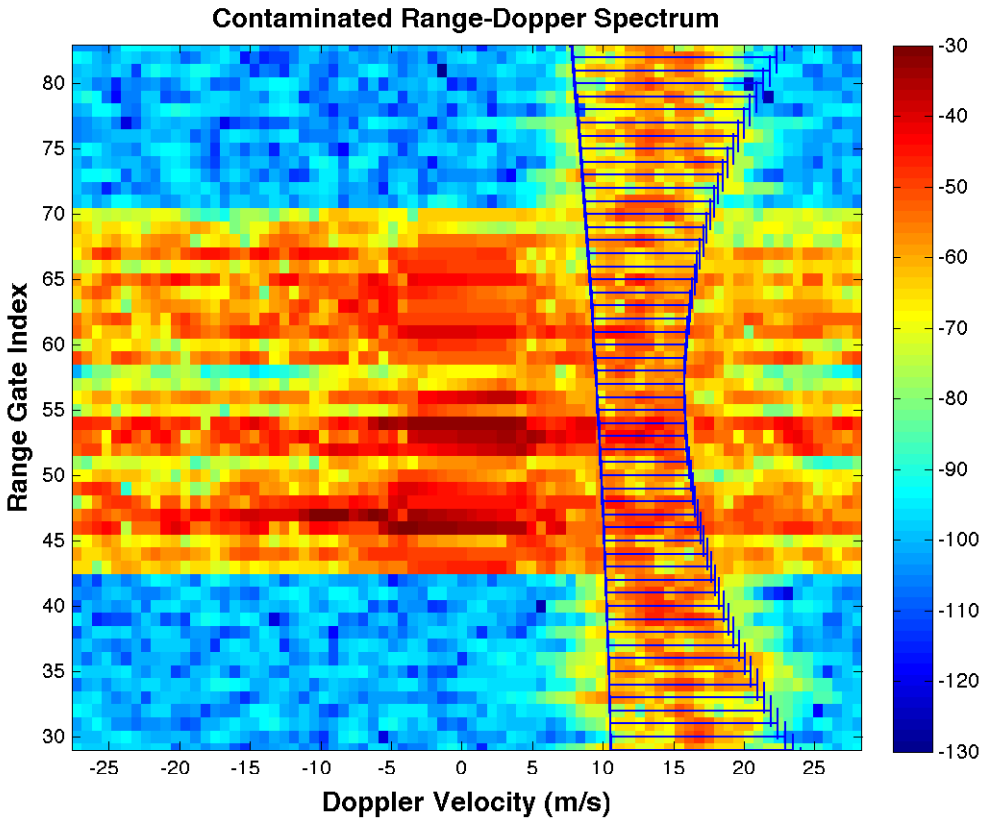

Figure 2.4: Contaminated range-Doppler spectrum and the estimated weather window. The weather window attempts to capture the spectral coefficients that are most likely related to the weather signal in the contaminated gates.

detection method is presented in Section 2.3.2, and the limitations of the method are described in Section 2.3.3.

2.3.1 Motivation for EDM

The EDM focus on the transitions from non-contaminated gates to contaminated gates to estimate the weather window. In a WTC-contaminated range-Doppler spectrum, there are three types of frequency bins depending on the signal content of that bin: weather-signal bins, noise bins, and WTC bins. Weather-signal bins are the frequency bins containing power from the weather signal only or bins containing power from weather signal and WTC signal; noise bins are bins containing power from noise only; and WTC bins are the frequency bins containing power from WTC signal only. Observing the contaminated range-Doppler spectrum in Figure 2.4, a key characteristic of WTC contamination is the widespread of high power over the majority of frequency bins. As a result, there is a jump in power level from noise bins to WTC bins. On the contrary, power changes from WTC bins to WTC bin, weather-signal bins to weather-signal bins, and noise bins to noise bins are much smaller. The large power changes from noise bins to WTC bins allow the transition from a non-contaminated gate to a contaminated gate to be modeled as a step edge. A mitigation technique based on edge detection can be developed to identify the weather window because the spectral coefficients inside the weather window should have weather to weather transition instead of noise to WTC transition.

A major advantage of the EDM is that it does not require prior knowledge of which gates are contaminated by WTC. The algorithm can perform both detection and mitigation of WTC contamination. However, for this mitigation technique to perform well, three key assumptions must hold. The first assumption is that the weather signal must be continuous in range; in other words, the weather signal must have similar velocity and spectrum width from gate to gate. The second assumption is that the transition from non-contaminated gate to contaminated gate must fit the step edge model. The last assumption is that the clutter-to-signal ratio (CSR) must be small to ensure the power level change from weather-signal bins in a non-contaminated gate to weather-signal bins in a contaminated gate is small. While the first assumption is common to all range-Doppler spectrum-based WTC mitigation methods, the second and third assumptions are unique to the edge detection method and place a significant constraint on the applicability of the method. Section 2.3.3 will discuss the limitations of the edge detection method in detail.

2.3.2 EDM Algorithm Description

There are four inputs to the edge detection method: the contaminated range-Doppler spectrum, the aliasing velocity, the data window used to estimate the spectrum, and the noise power level. Following the flow chart for the edge detection method shown in Figure 2.5, the first step of the algorithm is to form a block of four range gates as a "processing unit". The processing unit consists of a reference gate,

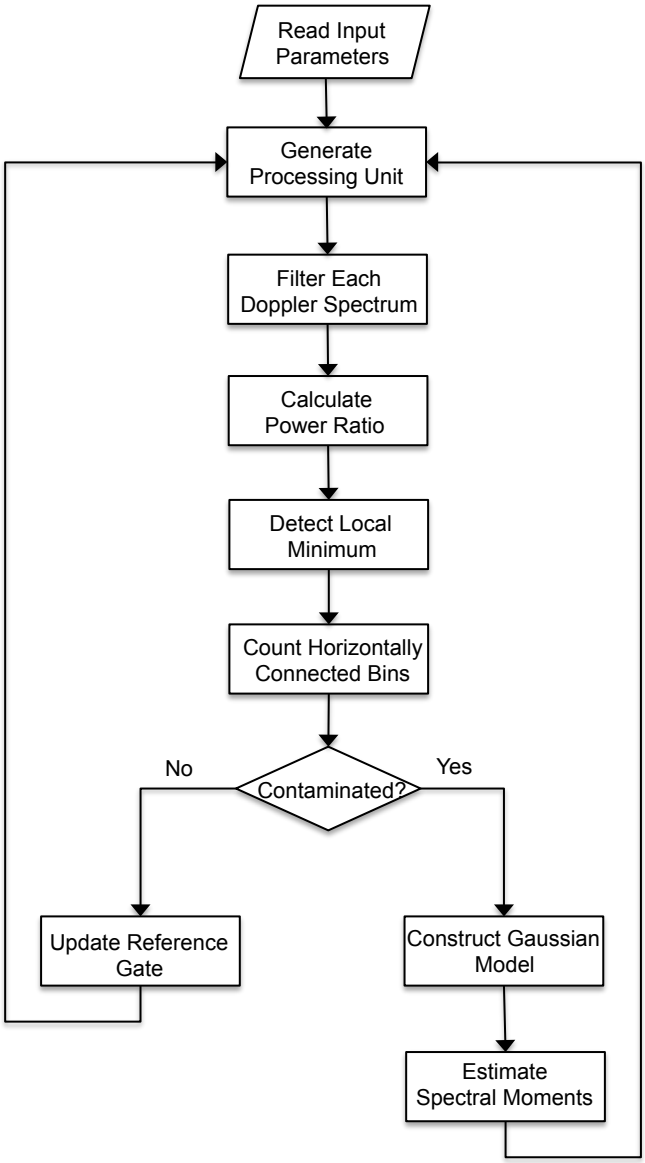

Figure 2.5: Flow chart of the EDM. The algorithm iteratively remove WTC contamination one gate at a time by detecting the noise bin to WTC bin transitions in the range-Doppler spectrum.

a testing gate, the gate immediately before the reference gate, and the gate immediately after the testing gate. An example processing unit is shown in Figure 2.6. In this example, the first spectrum from the bottom is from the gate before the ref-

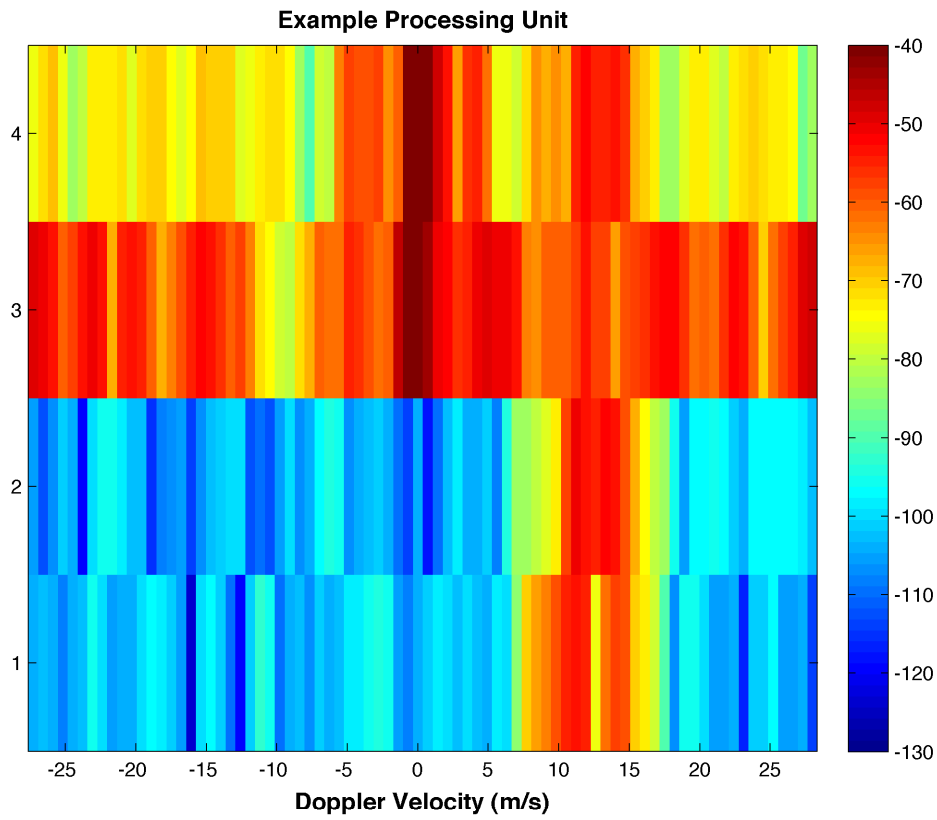

Figure 2.6: Example processing unit used in the EDM. This processing units shows the transition from a non-contaminated reference gate (second spectrum from the bottom) to a contaminated testing gate (third spectrum from the bottom).

erence gate, the second spectrum is from the reference gate, the third spectrum is from the testing gate, and the fourth spectrum is from the gate after the testing gate. After generating the processing unit, the power ratio, PR, of each frequency bin is calculated following gate pairs: the reference gate and the gate before it, the testing gate and the reference gate, the gate after the testing gate and the testing gate. The power ratio at frequency bin v between two range gates with discrete indices n_o and n is defined as

$$PR(v, n_o, n) = \frac{10 \log_{10}(S(v, n))}{10 \log_{10}(S(v, n_o))} \tag{2.2}$$

where $S(v, n)$ is the Doppler spectrum for the nth range gate in the range-Doppler spectrum. In the processing unit, there are four types of transitions: noise bin to noise bin, weather-signal bin to weather-signal bin, WTC bin to WTC bin and noise bin to WTC bin. The first three types of transitions have small power changes and produce power ratios close to 1, while the noise to WTC transitions have a large power change and produce power ratios much smaller than 1. A five-point average

in frequency is applied to the Doppler spectra before calculating the power ratio to reduce fluctuations of the spectral coefficients due to the variance of the periodogram spectral estimator. The power ratios for the example processing unit are shown in Figure 2.7. The bottom row of Figure 2.7 is the power ratio between the reference

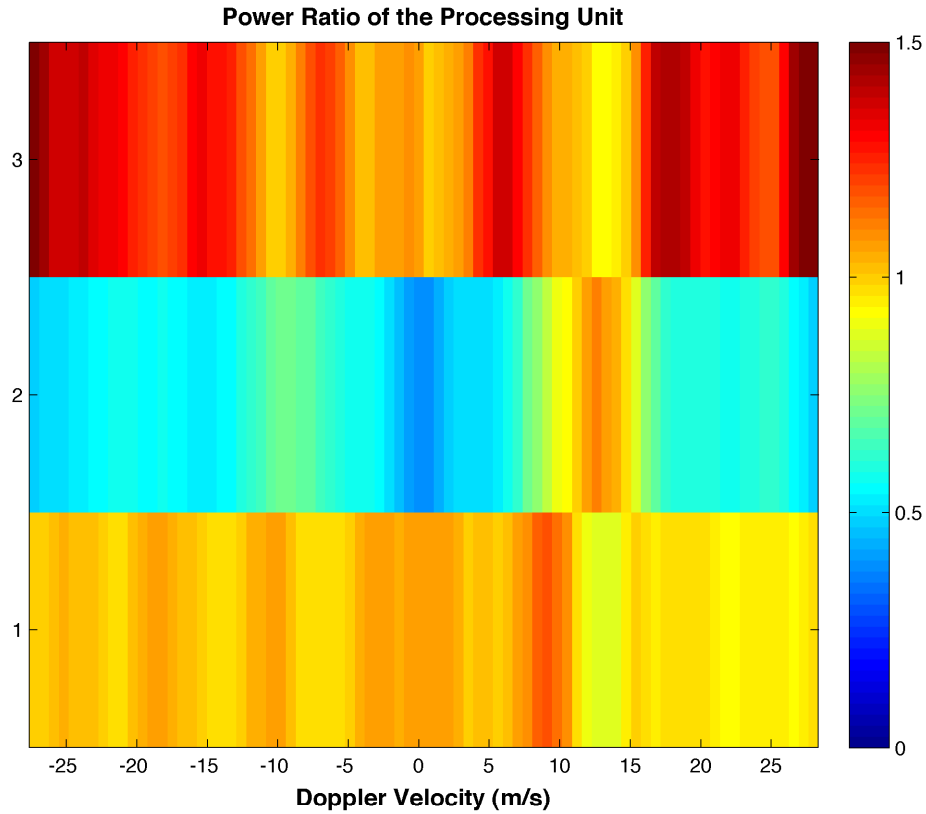

Figure 2.7: Power ratio of the processing unit shown in Figure 2.6. The x-axis is Doppler velocity and the color represents the power ratio in each frequency bin between two consecutive rows in the processing unit.

gate and the gate before it. Since the transitions between those two gates are either noise to noise or weather to weather, the expected power ratio for each frequency bin is 1. The second row of Figure 2.7 is the power ratio between the testing gate and the reference gate. According to Equation (2.2), a step up transition from noise to WTC will produce power ratio much lower than 1. The top row of Figure 2.7 is the power ratio between the testing gate and the gate after it. Since the gate after the testing gate has lower power in most frequency bins in the example processing unit, the expected power ratios for those bins are greater than 1. The power ratios shown in Figure 2.7 match the expected power ratios. Since the exact value of power ratio depends on the WTC power and noise power, it is difficult to set a hard threshold on the power ratio to detect which bins are WTC bins. A better approach is to use the fact that noise to WTC transitions generate extreme values in power ratio. Since the edge detection method is applied from the closer range gates to the farther range gates, the only type of noise to WTC transitions expected are step up edges which

produce power ratios that are local minima. The local minima detection result is shown in Figure 2.8. The middle row of Figure 2.8 is the detection result on the

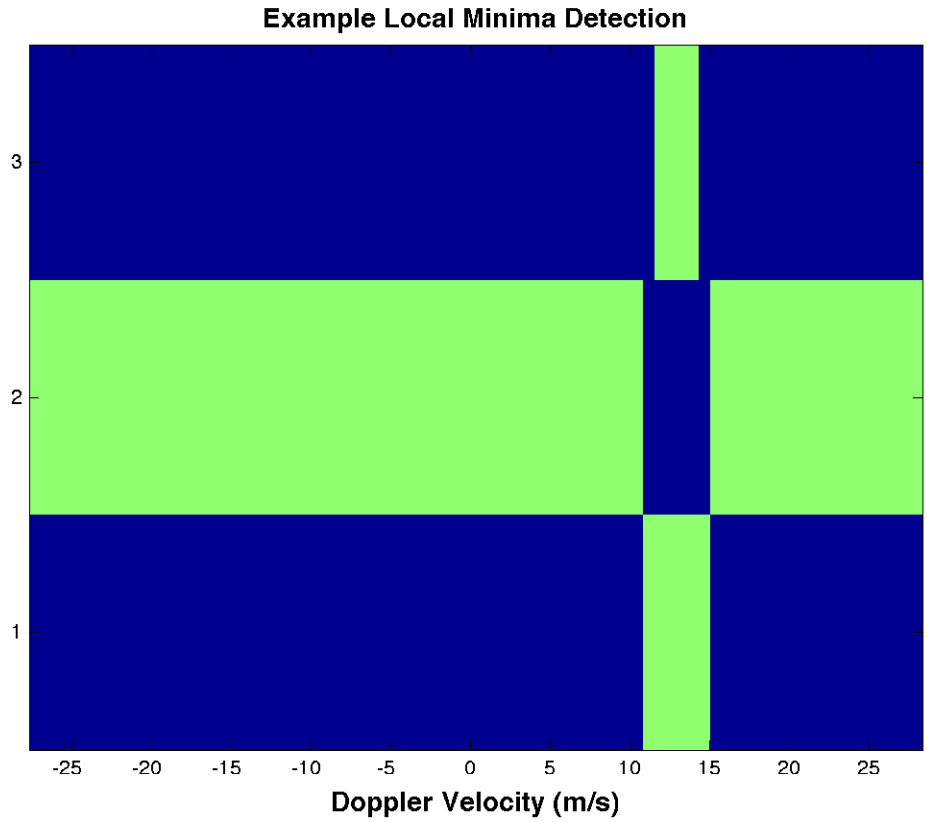

Figure 2.8: Local minimum detection result on the power ratio shown in Figure 2.7. The light green bins in row 2 indicate which bin in the testing gate are WTC bins. The detections in row 1 and 3 are disregarded by the algorithm because they do not correspond to WTC bins.

testing gate in the example processing unit shown in Figure 2.6 and the light green bins correspond to the WTC bins in the testing gate. The bins in the top and bottom row that are detected as local minima because the power ratios in those frequency bins are smaller than the power ratio in the same frequency bins of the middle row. Since only the local minima detection on power ratios between the reference gate and the testing gate is of interest, the detections in the top and bottom row of Figure 2.8 are disregarded by the EDM.

Two potential sources of false detections must be taken into consideration: the fluctuations in the power ratio and the transition from noise to weather. The false detections due to power ratio fluctuations are removed by requiring the detected minima to have a power ratio lower than a conservative threshold. Since WTC signals have much larger spectrum width than normal weather signals, a true WTC-contaminated gate can be expected to have a higher number of horizontally connected bins that are labeled as potential WTC bins than a false detection case resulting from noise to weather transitions. Therefore, a method to remove false detections from

noise to weather transitions is to apply a threshold on the length of the detected edge, which is defined as the number of horizontally connected bins that are labeled as potential WTC bins. If the testing gate in the processing unit has more than 35% of its bins labeled as WTC bin, it will be considered as contaminated. In the example processing unit, there are no false detection and the result after applying the power ratio threshold and length threshold is the same as the detection shown in Figure 2.8. The testing gate in the example is detected as contaminated.

If the testing gate is detected as contaminated, a Gaussian model for the weather signal is constructed using the signal power and velocity estimated using the non-WTC bins from the contaminated gate. The spectrum width used to build the model is estimated from the reference gate. The spectral moments are then estimated using the model spectrum. If the testing gate is labeled as non-contaminated, it is designated as the new reference gate, otherwise the reference gate stays the same. The procedure is then repeated for a new processing unit containing the reference gate and a testing gate shifted in range by one gate. The whole mitigation process is terminated after each range gate is processed as the testing gate. Figure 2.9 shows

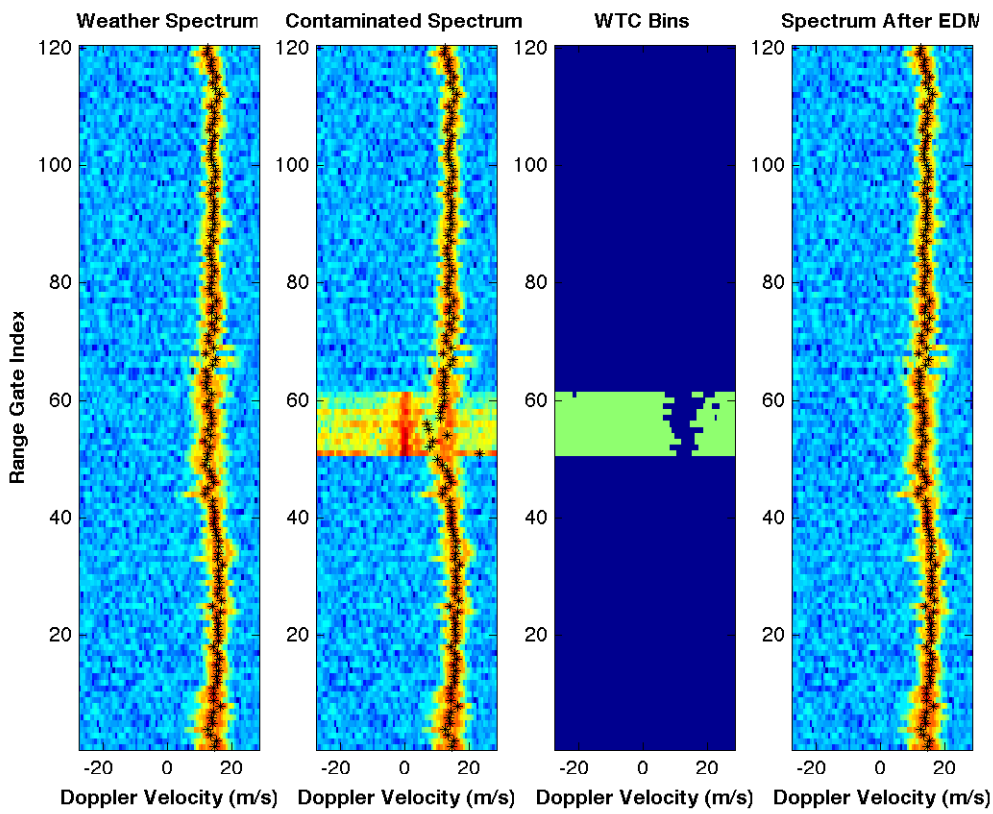

Figure 2.9: The weather spectrum (left), contaminated spectrum (middle left), WTC bins (middle right), and the spectrum after applying EDM (right). Most of the WTC bins in the contaminated spectrum are detected as shown in the WTC bins plot.

an example mitigation result using this method. The left panel shows the uncontaminated weather spectrum; the middle left panel shows the WTC-contaminated

spectrum; the middle right panel shows the frequency bins labeled as WTC bins; and the right panel shows the spectrum after applying EDM. Comparisons between the spectrum after filtering and the uncontaminated weather spectrum shows that the EDM significantly improved the radial velocity estimates in the contaminated gates while preserving the original estimates in the the non-contaminated gates. Visual inspection of the spectrum after EDM shows that the spectrum width and power biases in the contaminated gates are reduced as well.

2.3.3 Limitations of EDM

The edge detection method also has several limitations that constrain its applicability and performance under certain conditions. One major limitation is the need for a reference gate. To satisfy the weather continuity assumption, it is desirable to use a non-contaminated gate that is closest to the contaminated gate as the reference gate. This implies the reference gate must be updated after each iteration of the algorithm depending on the detection result of the testing gate. However, if the algorithm missdetects a contaminated gate, the reference gate will be updated to a contaminated gate, and no mitigation will be done on the remaining contaminated gates because there is no sharp transition from contaminated gate to contaminated gate. The iterative nature of the algorithm dictates that any error will be propagated to the next iteration and potentially resulting in complete failure of the algorithm. The iterative approach also makes the algorithm more computationally complex, which is undesirable in an operational setting.

The difficulty in maintaining a good reference gate is not the only limitation on the edge detection method, the strong dependence on the assumptions stated in Section 2.3.1 also severely limits the cases where the algorithm is applicable. There are cases of WTC contamination that do not satisfy the step edge requirement. An example of such contamination and the mitigation result is shown in Figure 2.10. In this example, the WTC contaminations in range gates 42 to 46 are successfully removed by the edge detection method, but the contaminations in range gates 50 to 60 and 64 to 70 is not mitigated by the method. The algorithm failed because the power of each contaminated gate is stronger than the contaminated gate before it, resulting in a ramp edge instead of a step edge.

The algorithm also performs poorly when the small CSR assumption is violated, as shown in Figure 2.11. In this example, the transition from bins containing only weather signal to bins containing weather and WTC signal also satisfy the step edge model. This results in all bins of the contaminated gate being labeled as WTC bins and no weather window is produced, which leads to the weather information in the contaminated gates to be completely removed. The limited applicability of the EDM and its potential for catastrophic errors make the technique an ineffective solution to the WTC problem. Another algorithm that takes advantage of the range-Doppler spectrum but without some of the limiting assumptions of the EDM is presented next.

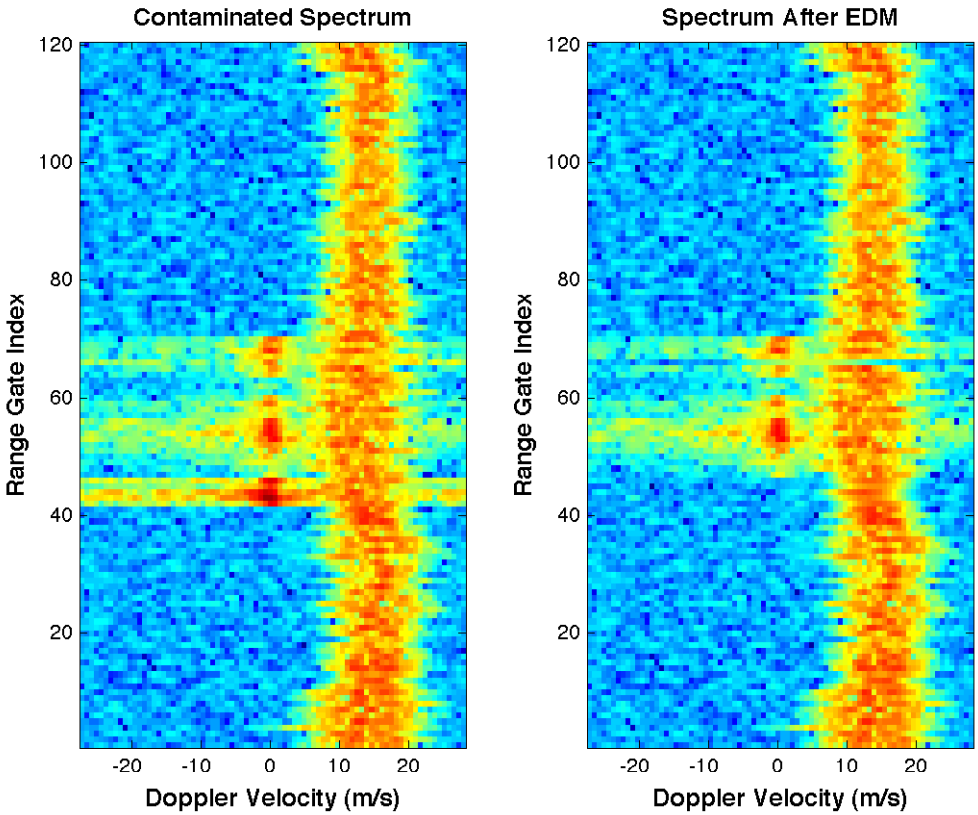

Figure 2.10: Example of contaminated spectrum with both step and ramp noise-to-WTC transitions and corresponding filtered spectrum (right). Gates 42 to 46 have step edge noise-to-WTC transitions while gates 50 to 60 and 64 to 70 have ramp noise-to-WTC transitions.

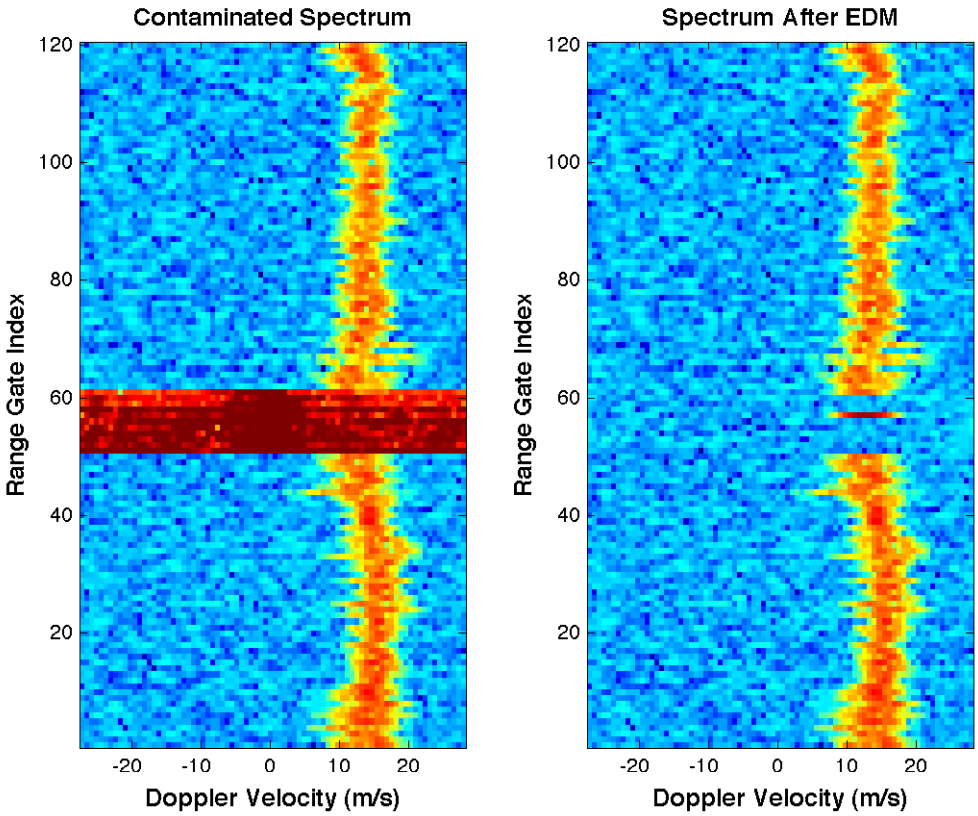

Figure 2.11: Example of contaminated spectrum with high CSR and corresponding filtered spectrum (right). Weather-signal bins in the contaminated range gates are detected as WTC bins in range gates 51 to 61resulting in weather signal being lost for those range gates.

2.4 Range-Doppler Regression

To address the limitations of the edge detection method presented in Section 2.3, a new method using the range-Doppler spectrum is developed. The range-Doppler regression (RDR) method does not focus on the discontinuities caused by the WTC in range, instead it relies on the continuity of weather signals in range. The RDR method still follows the steps a human expert would take to estimate the spectral moments for the contaminated gates described in Section 2.2. This section will discuss the advantages and assumptions of the RDR method, present a detailed description of the algorithm, and describe the limitations of the RDR method.

2.4.1 Motivation for RDR Algorithm

Since the EDM developed in Section 2.3 did not produce satisfactory results for a number of different cases, a more effective mitigation technique is developed to take advantage of the range-Doppler spectrum. Instead of comparing a non-contaminated gate and a contaminated gate bin by bin to determine the proper location of the weather window, low-order polynomial fits using velocity and spectrum width information from neighboring non-contaminated gates are used to estimate the weather window. The first advantage the RDR algorithm has over the EDM is that the polynomial fits can follow the local trends in velocity and spectrum width of the weather signals, which allows for the weather window to shift in frequency from range gate to range gate. Therefore, the RDR method can better handle weather conditions with velocity shear. The second advantage of the RDR method is that the need of a reference gate is eliminated because each neighboring non-contaminated gate will contribute to the fits. The third advantage of the RDR method is that the weather window estimation process is independent of the CSR. Like the EDM, the RDR algorithm does not affect the non-contaminated gates.

Besides the weather continuity assumption that is common to both range-Doppler spectrum-based mitigation methods, the RDR method also requires approximate knowledge about which range gates are contaminated by WTC. Without such knowledge, the velocity and spectrum width from contaminated gates could be used to perform the fits, which could significantly reduce the accuracy of the estimated weather window. However, there are several methods to generate the required WTC contamination information. An automatic WTC detection algorithm was recently developed by Hood et al. (2010) that can be used to detect the location of WTC before applying the RDR method. A conservative estimation of contaminated gates based on the known locations of the wind turbines can also be used because the biases introduced by the RDR algorithm in non-contaminated gates that are treated as contaminated are small. As a result, requiring approximate knowledge of contaminated gates does not place a significant constraint on the applicability of the RDR mitigation method.

2.4.2 RDR Algorithm Description

The inputs to the RDR method are the contaminated range-Doppler spectrum, the approximate location of the contaminated gates, the aliasing velocity, the data window used to estimate the spectrum, and the noise power level. Following the flow chart of the algorithm shown in Figure 2.12, the first step in the RDR method is to

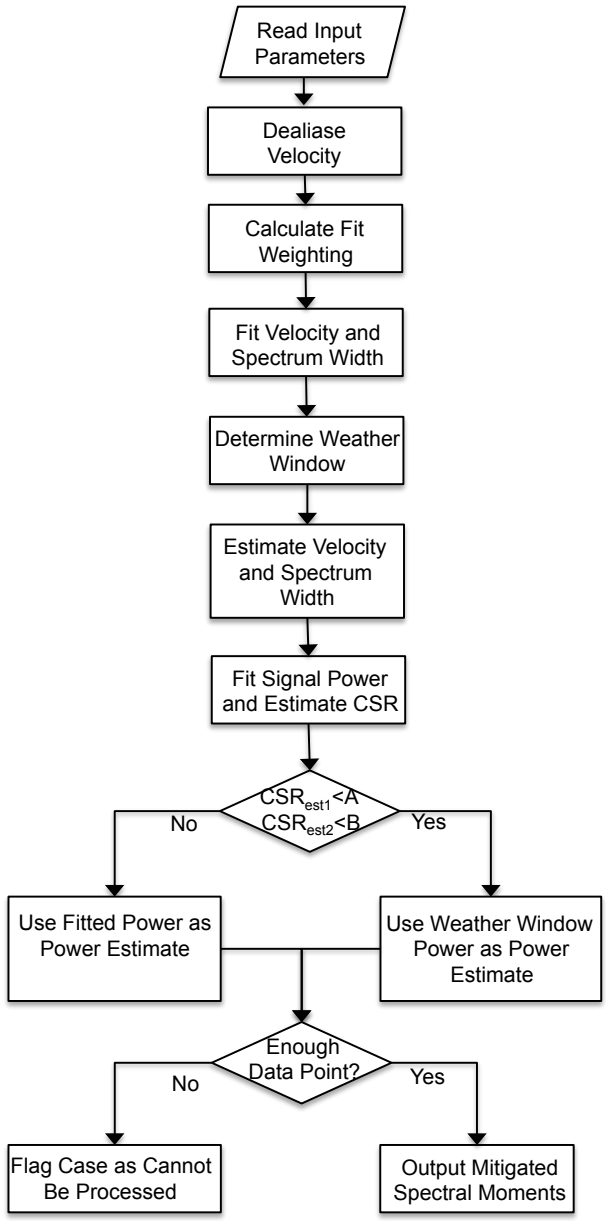

Figure 2.12: The flow chart for the RDR algorithm. The RDR algorithm uses low order polynomial fits to determine the weather window and estimates the spectral moments based on the weather window. The weather signal power estimates are then adjusted based on estimated CSR.

estimate the spectral moments using the contaminated range-Doppler spectrum and

dealias the velocities from the non-contaminated gates using a seven point running window dealiasing algorithm. For each range gate, the velocity is dealiased based on the following rule:

$$v_d(n) = \begin{cases} v(n) + 2v_a & v(n) - v_{med} < -v_a \\ v(n) - 2v_a & v(n) - v_{med} > v_a \\ v(n) & \text{otherwise} \end{cases} \tag{2.3}$$

where $v(n)$ is the velocity estimate at the nth range gate, $v_d(n)$ is the dealiased velocity, and v_{med} is the median velocity of the seven range gates in the running window. If velocities from contaminated gates would be included in the running window, the velocities from the non-contaminated gates immediately after the contaminated gates are used instead. After velocity dealiasing, low-order polynomial fits for velocity and spectrum width are done using weighted velocity and spectrum width data from the non-contaminated gates. Since the velocity and spectrum width fits will be used to determine the weather window, a low-order fit is enough to capture the local trends in the weather signal. An example of the velocity and spectrum width fits is shown in Figure 2.13. The requirement of knowing which gates are contaminated is evident

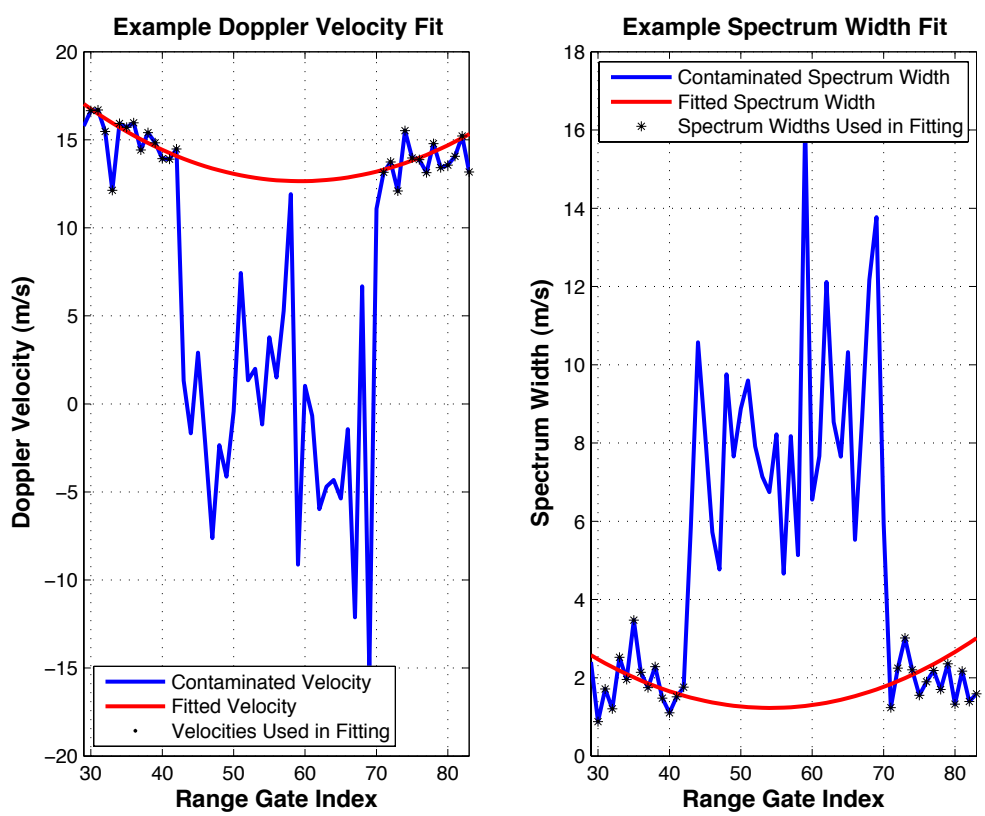

Figure 2.13: Velocity fit (left) and spectrum width fit (right). The blue curves are the contaminated velocity and spectrum width estimates, the red curves are the fitted velocity and spectrum width using the non-contaminated velocity and spectrum width estimates indicated by the black *.

since velocities and spectrum widths from the contaminated gates are wildly different from the neighboring non-contaminated gates and cannot be used to generate the fits. Both fits shown in Figure 2.13 are second order.

The weights used in the fit are the multiplication of two separate weights based on signal-to-noise ratio (SNR) and proximity to the contaminated gates. The SNR weight is calculated using a binary threshold as follows:

$$W_{SNR}(n) = \begin{cases} 1 & SNR(n) > T_{SNR} \\ 0 & SNR(n) \leq T_{SNR} \end{cases} \tag{2.4}$$

where $W_{SNR}(n)$ is the SNR weight at the nth range gate, $SNR(n)$ is the SNR at the nth range gate, and T_{SNR} is the SNR threshold. Since only range gates with significant weather return will receive nonzero SNR weight, the SNR weight prevents velocity and spectrum width from range gate with only noise signal to contribute to the fit. The second weight is based on the proximity of the range gate to the contaminated range gates. It is given by

$$W_{prox}(d) = \begin{cases} \frac{1}{2}\left(1 + \cos\left(\frac{\pi}{T_{prox}} d\right)\right) & 0 \leq d \leq T_{prox} \\ 0 & \text{otherwise} \end{cases} \tag{2.5}$$

where d is the distance between the current range gate and the closest contaminated range gate measured in number of range gates, $W_{prox}(d)$ is the proximity weight for distance d, and T_{prox} is the threshold after which the proximity weight will be zero. The proximity weight allows range gates that are closer to the contaminated gate to contribute more to the fitting than range gates that are farther away. The unequal contribution makes the fitting follow the local weather trend and reduces the polynomial order needed to accurately estimate the location of the weather window. Figure 2.14 shows the weights used to produce the fits shown in Figure 2.13. The SNR weight on the left panel of Figure 2.14 were calculated using $T_{SNR} = -2$ dB and it is 1 for all non-contaminated gates because this example was produced from a stratiform precipitation condition and there were no gates with non-significant weather returns. The proximity weights shown in the middle panel of Figure 2.14 were calculated using $T_{prox} = 13$. The optimum thresholds for the weights are determined in Section 3.2.1.

Once the fitting is completed, the resulting polynomial coefficients are used to estimate the center and width of the weather window for the contaminated gates. The two limits defining the weather window for a range gate are given by

$$\hat{v}(n) - K\hat{w}(n) \tag{2.6}$$

and

$$\hat{v}(n) + K\hat{w}(n) \tag{2.7}$$

where $\hat{v}(n)$ and $\hat{w}(n)$ are the fitted velocity and spectrum width at the nth range gate, respectively, and K is the weather window width factor. Figure 2.15 shows the weather window determined using the fitting in Figure 2.13 and Equation (2.6) and (2.7). Assuming the weather signal is continuous in range, the estimated weather window in the contaminated gates should include most of the weather spectral coefficients

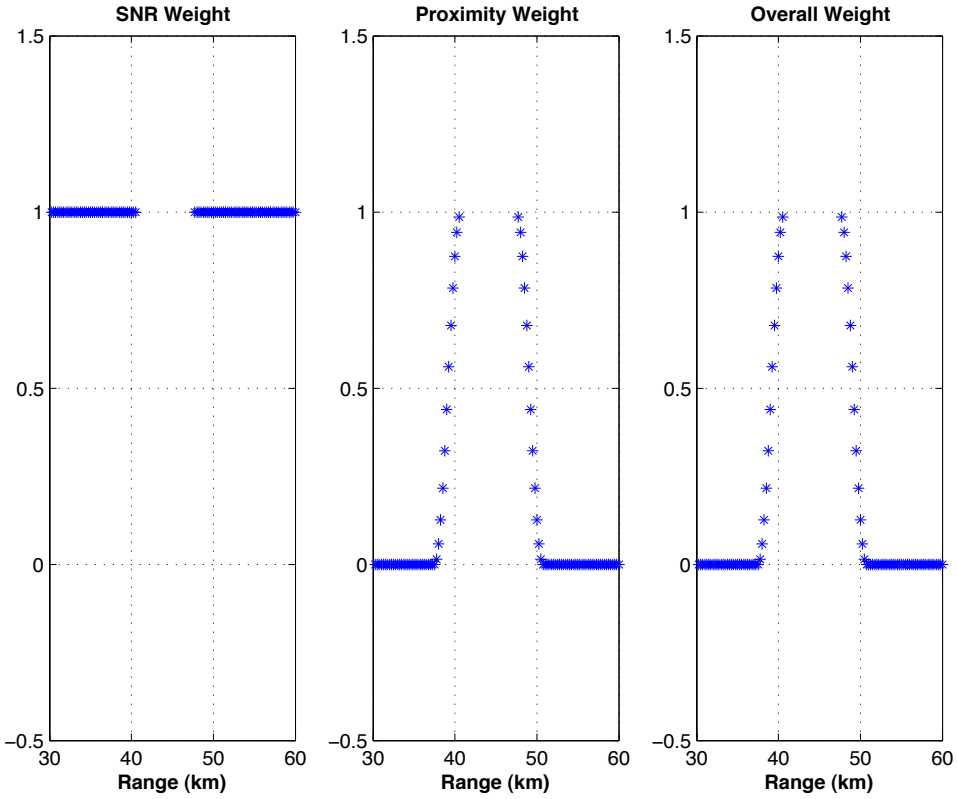

Figure 2.14: SNR weight (left), proximity weight (middle), and the overall weight (right). For any range gate, the SNR weight is determined using a binary threshold, the proximity weight is determined using a cosine roll off given by Equation (2.5), and the overall weight is the multiplication of the SNR weight and the proximity weight.

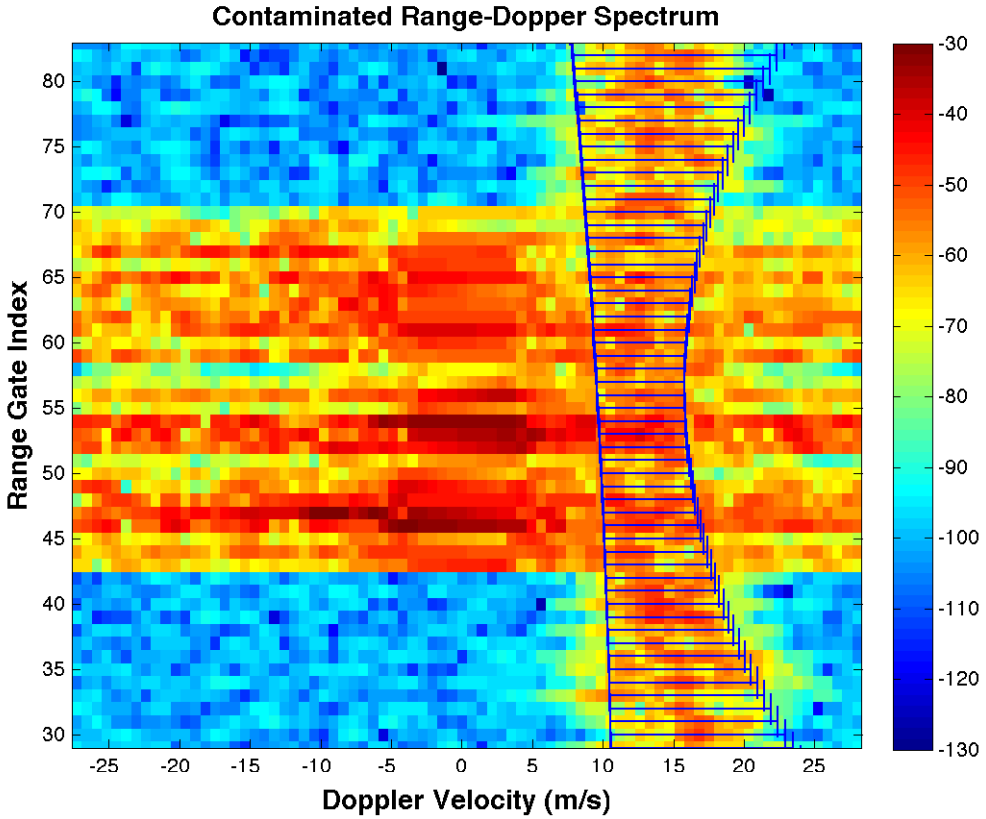

Figure 2.15: Contaminated range-Doppler spectrum and the estimated weather window. The horizontal bars indicate the estimated weather windows.

since the estimated weather window does a good job capturing the weather spectral coefficients in the non-contaminated gates neighboring the contaminated gates.

After determining the weather window, spectral moments are estimated using only the spectral coefficients inside the weather window. For velocity and spectrum width, the new estimates have significantly less bias than the contaminated spectrum as will be shown in Chapter 3. However, signal power estimates are still biased because each spectral coefficient inside the weather window also contains WTC power. The degree of power bias depends on the CSR. For low CSR, the WTC power contained in each spectral coefficient is small, and the power estimates produced using the weather window have a small bias. For high CSR, the WTC power contained in the spectral coefficients is much larger than the weather signal power, and the power estimates produced by the weather window still have unacceptable biases. Ideally, a threshold on CSR can be set such that any cases with lower CSR will use the weather window estimates, and other cases will use power estimates from a weighted low-order polynomial fit using neighboring non-contaminated signal power estimates. In practice, the true CSR for each contaminated gate is unknown and simple thresholding is ineffective.

To compensate for the lack of knowledge about the true CSR, two estimators for CSR are developed:

$$CSR_{est1}(n) = 10\log_{10}\left(\frac{S(n)}{\hat{S}(n)}\right) \tag{2.8}$$

and

$$CSR_{est2}(n) = 10\log_{10}\left(\frac{S(n) - \tilde{S}(n)}{\tilde{S}(n)}\right) \tag{2.9}$$

where for the nth range gate, $S(n)$ is the total power estimated using the contaminated spectrum, $\tilde{S}(n)$ is the power estimated using the weather window, and $\hat{S}(n)$ is the power estimated from a weighted polynomial fit. For the high CSR cases, CSR_{est1} should produce good estimates because the WTC signal overpowers the weather signal and $S(n)$ is a good estimate of the clutter power, while $\hat{S}(n)$ is the best estimate for weather power. CSR_{est2} should gives better estimates for the low CSR cases because in this situation the best estimator for weather signal power is $\tilde{S}(n)$, and the clutter power is the total contaminated power minus the weather signal power. Figure 2.16 plots the estimated CSR against the true CSR for both estimators using simulated contaminations. The left panel shows the performance of the CSR estimators for stratiform precipitation and the right panel shows the performance for convective storm. In both cases, CSR_{est1} underestimates the true CSR for cases with true CSR greater than 0 dB because the true CSRs are calculated before applying the GCF and CSR estimates are made after applying the GCF. For cases with true CSR less than 0 dB, CSR_{est1} asymptotically approaches 0 dB because $S(n)$ is dominated by the weather signal power at low CSRs. For CSR_{est2}, it saturates to a fixed number that is dependent on the window width factor when the true CSR is high. The error bars indicates the standard deviation associated with each estimator for a fixed CSR. CSR_{est2} have slightly larger standard deviation for convective storm because it is

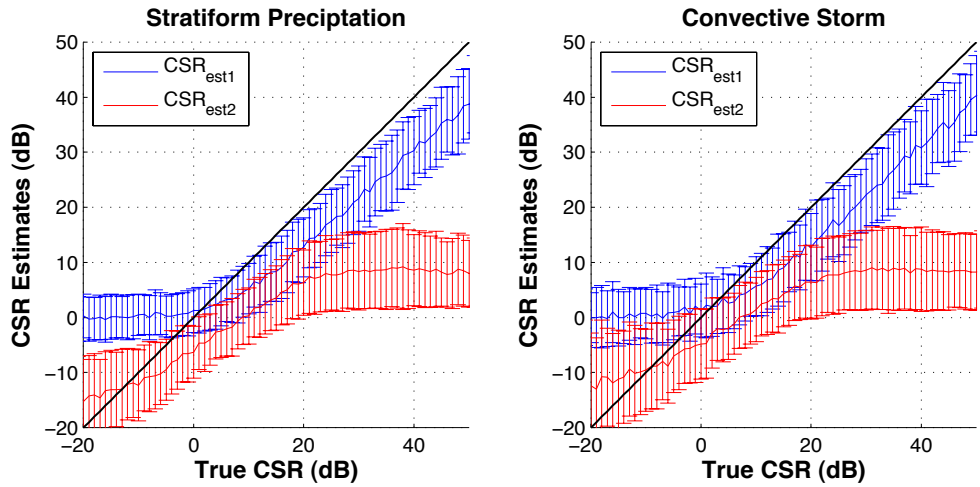

Figure 2.16: Estimated CSRs plotted against the true CSRs for stratiform precipitation (left) and convective storm (right). The error bars indicate the standard deviation of the estimations. Because of the large standard deviation associated with each estimator, both estimators are needed to determine whether the power estimate from the weather window or the power estimate from a fit should be used as the weather signal power estimate.

more difficult to accurately estimate the weather window due to the typical velocity shear.

Using only CSR_{est1} to determine how to estimate the weather signal power is unsatisfactory because there are many cases where the true CSR is low but the estimated CSR is high. Similarly, using only CSR_{est2} also produces unsatisfactory results because there are many cases where the true CSR is high but the estimated CSR is low. The best solution is to threshold both CSRs independently and use the following rule to determine whether $\tilde{S}(n)$ or $\hat{S}(n)$ should be the weather signal power estimates:

$$\text{Weather Signal Power Estimate} = \begin{array}{ll} \tilde{S}(n) & CSR_{est1} < A \text{ and } CSR_{est2} < B \\ \hat{S}(n) & \text{otherwise} \end{array} \tag{2.10}$$

where A is the threshold for CSR_{est1} and B is the threshold for CSR_{est2}. To catch the cases where there is no contamination or extremely weak contamination, no mitigation will be performed if CSR_{est2} for a range gate is below -10 dB.

The last step in the algorithm is to flag the cases where there are not enough non-contaminated data points to perform the fitting. A case is flagged if there are fewer than three non-contaminated gates with weather signal either before or after the contaminated gates. Figure 2.17 shows the mitigation result for a stratiform precipitation case. The three panels show the non-contaminated weather spectrum, the contaminated spectrum, and the spectrum after applying the RDR algorithm, respectively. Comparing the weather spectrum to the spectrum after filtering, the RDR method successfully located the weather spectral coefficients in the contaminated gates and the new velocity estimates are closer to the uncontaminated velocity

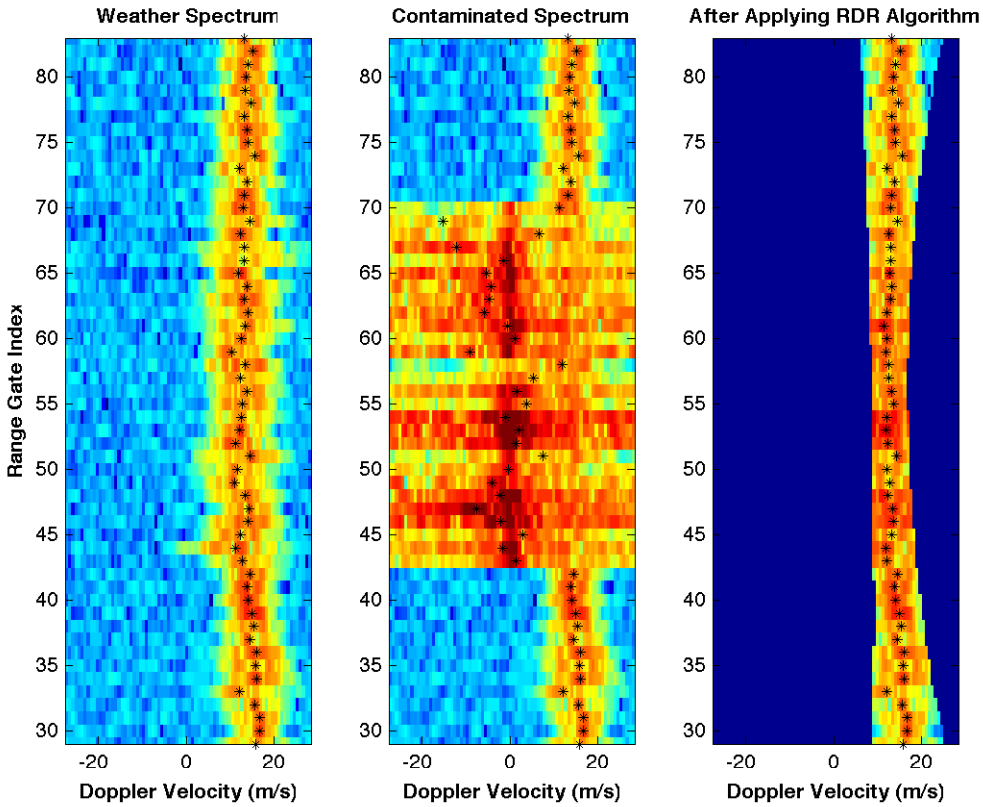

Figure 2.17: The weather spectrum (left), contaminated spectrum (middle), and the spectrum after applying the RDR algorithm (right) for a stratiform precipitation example. The velocity estimates, are indicated by the black stars. Visual inspection shows that the biases in the spectral moment estimates are reduced.

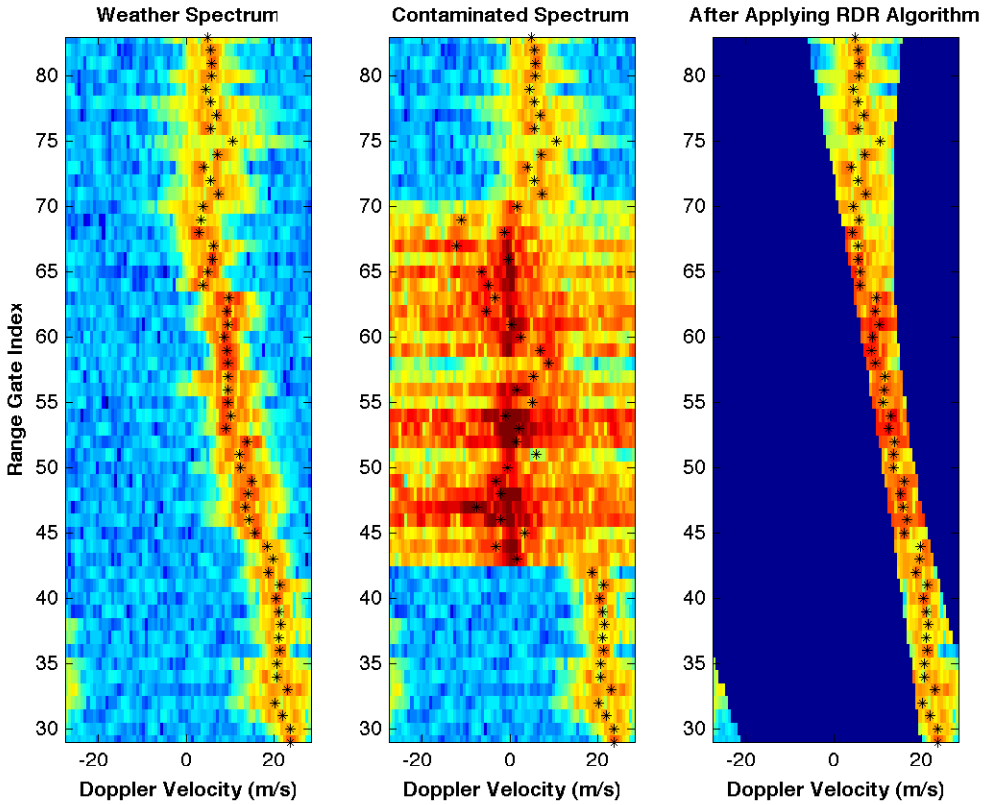

Figure 2.18: Same as Figure 2.17 except for a convective storm case. The velocity shear is handled well by the RDR method.

estimates. Figure 2.18 shows the mitigation results for a convective storm case to demonstrate that the RDR method can also handle cases with velocity shear. Qualitatively, it is clear that the RDR method can reduce the biases in the spectral moment estimates. Chapter 3 will present quantitative evaluation of the RDR method.

2.4.3 Limitations of RDR Algorithm

The RDR algorithm is a improvement over the the edge detection method described in Section 2.3, but it still has limitations. The fitting used to estimate the weather window is a major limiting factor. To produce the best fits, weather signals must be present at range gates before and after the contaminated gates. Without weather signals on both sides, the fit becomes an extrapolation using the local trend of the weather signal and could produce unrealistic weather window estimates. This situation should occur infrequently because the size of a weather system is usually much larger than the size of a wind farm, but motion of the weather system could cause the weather system to only partially overlap with the wind farm resulting in lack of weather signal to perform the fit. Another limitation of the algorithm is that the low-order polynomial fitting cannot capture a sudden large shift in velocity or spectrum width, which could occur near a tornado vortex. Fortunately, under such severe weather situations, most wind turbines will not be operating and will not cause WTC contamination.

Chapter 3

Simulations and Results

To quantitatively evaluate the performance of the range-Doppler regression (RDR) method described in Section 2.4, weather and wind turbine clutter (WTC) time series were simulated to test the RDR method for different weather conditions. Simulated data were selected over real data because simulations allows the complete control over important factors such as signal-to-noise ratio (SNR), clutter-to-signal ratio (CSR), the location of contamination, and the velocities and spectrum widths of the weather signal. By using simulated weather data, the true spectral moments of the weather signal without contamination, which are unavailable if real data were used, can be used to calculate the biases before and after mitigation. Section 3.1 will explain how the weather and WTC time series are simulated, Section 3.2 will present the process used to select the optimum parameters and the final mitigation performance, and Section 3.3 will show the mitigation result on real data set collected by WSR-88D, KOUN, located in Norman, OK.

3.1 Simulation Set Up

To fully evaluate the capability of the RDR method to mitigate WTC contamination, it must be tested under different weather conditions with different degrees of contamination. While some real data were available, they do not have the necessary variations to properly evaluate the mitigation method. Simulations, on the other hand, allows full control over SNR, velocity and spectrum width of the weather signal along with the CSR of the WTC signal. Simulated time series were used in Hood et al. (2010) to evaluate the automatic WTC detection algorithm and the result were satisfactory. This section will describe the weather and WTC simulations used in this work to evaluate the RDR method.

3.1.1 Weather Signal Simulation

Simulation of weather time series based on spectral shaping was first proposed by Zrnic (1975). However, this simulator can only simulate time series for a single range gate, which was insufficient for the purpose of evaluating the RDR mitigation method. The time series for a radial, which is consisted of all range gates along a single azimuth angle, can be simulated by simulating the weather signals for each gate individually. To ensure the variations of spectral moments from gate to gate are realistic, observed spectral moments from different weather conditions were selected manually to function as templates for the simulated weather. Using the observed weather signals as a basis, three parameters of the weather signals were changed during the simulation to generate the necessary variations to evaluate the RDR algorithm.

3.1.1.1 Observed Weather Signal

The observed weather signals were selected manually from observations of different weather conditions by WSR-88D, KTLX, located near Oklahoma City, OK. Stratiform precipitation and convective storm conditions were selected to be the basis weather signals because they presents a baseline case and a challenging case to test the RDR algorithm. Stratiform precipitation was the first weather condition to be simulated. Figure 3.1 shows a 120 range gate segment of the power, velocity, and

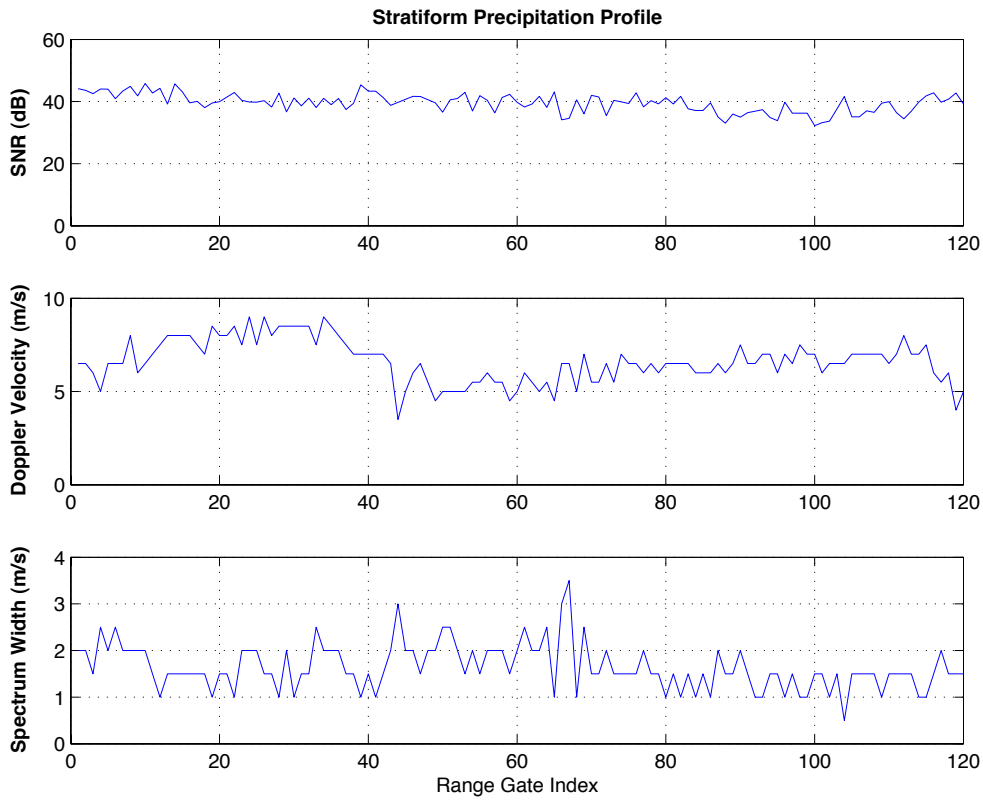

Figure 3.1: Stratiform precipitation profile. The power, velocity, and spectrum width of the observed weather signal is plotted as a function of range gate index with the smaller value indicating the range gate is closer to the radar. All three spectral moments display small fluctuations from gate to gate, but there are no significant changes through the selected range gates.

spectrum width of a stratiform precipitation event observed by KTLX on November 15, 2010, at 14:23 UTC with elevation 0.5 degree and azimuth 315 degrees. The three spectral moments shows small fluctuations from gate to gate but the overall trend over the whole range window is constant. The stratiform precipitation weather signal should provide a baseline performance evaluation of the RDR because it best satisfies the weather continuity assumption of the RDR algorithm. Figure 3.2 shows the selected profile for convective storm condition. This segment was selected from an event observed by KTLX on May 16, 2009, at 01:10 UTC with elevation 0.5 degree and azimuth 287 degrees. The power and velocity profiles show significant change

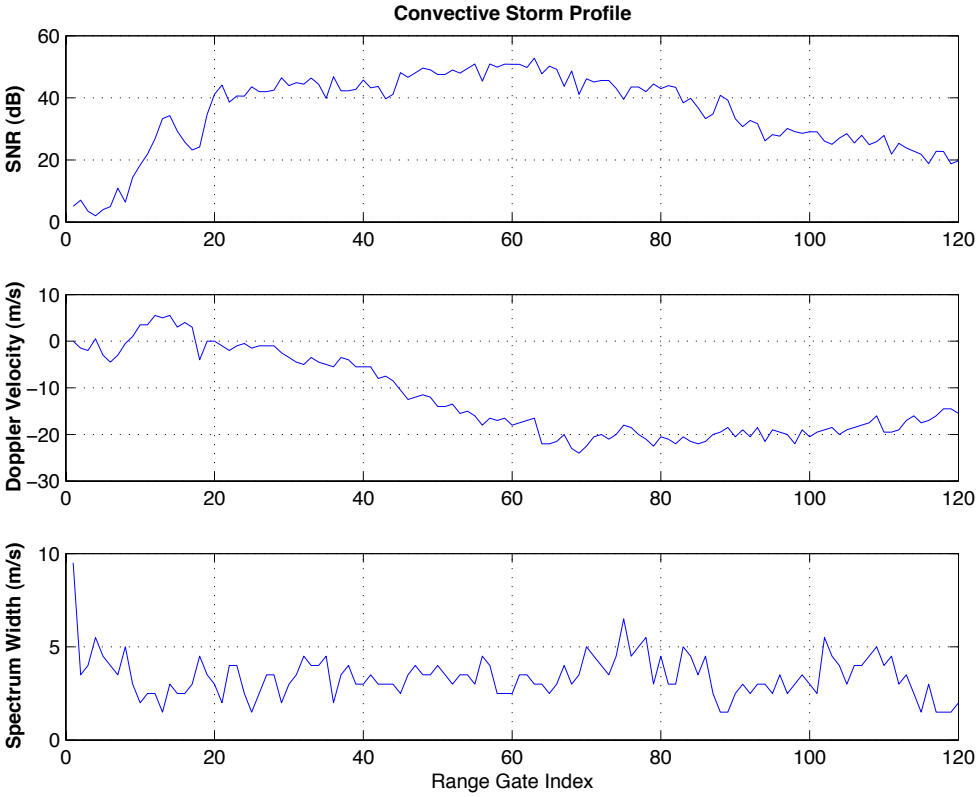

Figure 3.2: Same as Figure 3.1 except for convective storm condition. The power profile shows an increases from -100 dB to -55 dB then a decline to -80 dB, the velocity profile shows a large shear between range gate 20 and 60, and the spectrum width stays relative constant but is wider than the spectrum width in stratiform precipitation conditions.

within the selected range gates, which can challenge the RDR algorithm's capability to handle velocity shear and SNR variations. The selected stratiform precipitation and convective storm profiles cannot represent all possible weather signals, however, through proper scaling, a variety of different weather signals can be generated using the profiles shown in Figure 3.1 and 3.2.

3.1.1.2 Weather Simulation Parameters

The gate-by-gate weather time series simulator based on (Zrnic 1975) required seven input parameters for each range gate: the number of samples per time series, noise power, aliasing velocity, SNR, velocity, and spectrum width of the weather signal. The first three parameters were fixed in this work with $M = 80$, $N =$ -80 dB, and $v_a = 28$. The last three parameters for each range gate were determined from profiles generated from the observed weather signal. Three parameters were varied in this work to generate different weather profiles: mean velocity, mean spectrum width, and maximum SNR. The mean velocity is defined as the average of the radial velocities for all range gates in a profile and is calculated using

$$\overline{v} = \frac{1}{120} \sum_{n=1}^{n=120} v(n) \tag{3.1}$$

where $\overline{v}$ is the mean velocity of a profile, n is the index of the range gates, and $v(n)$ is the radial velocity at range gate n in the profile. A new velocity profile can be generated using

$$v'(n) = v(n) - \overline{v}_0 + \overline{v}_{sim} \tag{3.2}$$

where $\overline{v}_0$ is the mean velocity of the observed weather profile, $\overline{v}_{sim}$ is the mean velocity for the simulated profile, and $v'(n)$ is the simulated velocity at range gate n in the new profile. By only changing the mean velocity of a profile during simulation, the gate to gate variations in velocity for the simulated weather signal was the same as the original weather profile, which ensures the simulated weather signal had realistic small scale variations. Since the aliasing velocity of the simulated weather signals was 28 $\mathrm{m\,s^{-1}}$, the simulated values for $\overline{v}_{sim}$, listed in Table 3.1, were evenly distributed between -28 $\mathrm{m\,s^{-1}}$ to 28 $\mathrm{m\,s^{-1}}$to generate testing cases for all velocities.

Table 3.1: Parameter values used in weather simulations

Parameter Name	**Simulated Value**
Mean Velocity (m/s)	-25, -14, 0, 14, 25
Mean Spectrum Width (m/s)	1, 2, 4
Maximum SNR (dB)	20, 30, 40, 50, 60

The mean spectrum width is similarly defined as the the average of the spectrum width for all range gates in a profile and is calculated using

$$\overline{w} = \frac{1}{120} \sum_{n=1}^{n=120} w(n) \tag{3.3}$$

where $\overline{w}$ is the mean spectrum width of a profile and $w(n)$ is the spectrum width at range gate n in the profile. Since spectrum width must be negative, a shift of the mean spectrum width cannot be used to generate a new spectrum width profile, instead, the following rule was used to generate a new spectrum width profile

$$w'(n) = \begin{array}{ll} w(n) - \overline{w}_0 + \overline{w}_{sim} & \overline{w}_0 < \overline{w}_{sim} \\ \frac{0.1-\overline{w}_{sim}}{d_{min}} d(n) + \overline{w}_{sim} & \overline{w}_0 \geq \overline{w}_{sim} \end{array} \tag{3.4}$$

where

$$d(n) = w(n) - \overline{w}_0 \tag{3.5}$$

In Equation (3.4), $\overline{w}_0$ is the mean spectrum width of the observed weather profile, $\overline{w}_{sim}$ is the mean spectrum width of the simulated profile, d_{min} is the minimum of $d(n)$ over all n, and $w'(n)$ is the simulated spectrum width at range gate n in the new profile. If $\overline{w}_{sim}$ is greater than $\overline{w}_0$, then no spectrum width in the simulated profile will be nonpositive, and simple shifting of the mean spectrum width can be used to generate the new profile. Otherwise, a scaling factor was applied after subtracting $\overline{w}_0$ to ensure that the minimum spectrum width in the simulated profile is 0.1 $\mathrm{m\,s^{-1}}$. The gate to gate variations in spectrum width were changed by applying the scaling factor, but the differences were minimal and the new profiles were still realistic.

The last parameter that were adjusted in the simulations was the maximum SNR. The reason maximum SNR was used instead the mean SNR is that the mean SNR was not a good representation of the weather power in convective storm conditions due to the large power variations in range, as shown in Figure 3.2. Adjusting the maximum SNR of the profiles also prevented the simulated weather signals from having unrealistic power levels. The maximum SNR is adjusted through a linear mapping of signal powers given by

$$s'(n) = \frac{s_{max}^{sim} - N_{sim}}{s_{max} - N_0} \left(s(n) - N_0\right) + N_{sim} \tag{3.6}$$

where N_0 is the observed noise power, N_{sim} is the simulated noise power, s_{max} is the maximum observed weather power, $s(n)$ and $s'(n)$ are the weather power and simulated weather power at range gate n, respectively. s_{max}^{sim} is the maximum power in the simulated profile and is given by

$$s_{max}^{sim} = N_{sim} \times SNR_{max}^{sim} \tag{3.7}$$

where SNR_{max}^{sim} is the maximum SNR in the simulated weather profile. The SNRs of simulated weather signals are plotted against the SNRs of the observed weather signals in Figure 3.3. For stratiform precipitation, the SNRs of the simulated weather signal are related to the SNRs of the observed weather by a constant shift determined by SNR_{max}^{sim} and the maximum SNR of the observed weather signal, SNR_{max}. The same holds for convective storm when SNR_{max}^{sim} used to simulated the weather signal is larger than SNR_{max}. However, when S_{max}^{sim} is lower than SNR_{max}, the relationship between simulated SNR and observed SNR is divided into two regimes. For range gates with observed SNR higher than a threshold, the simulated SNR are a constant

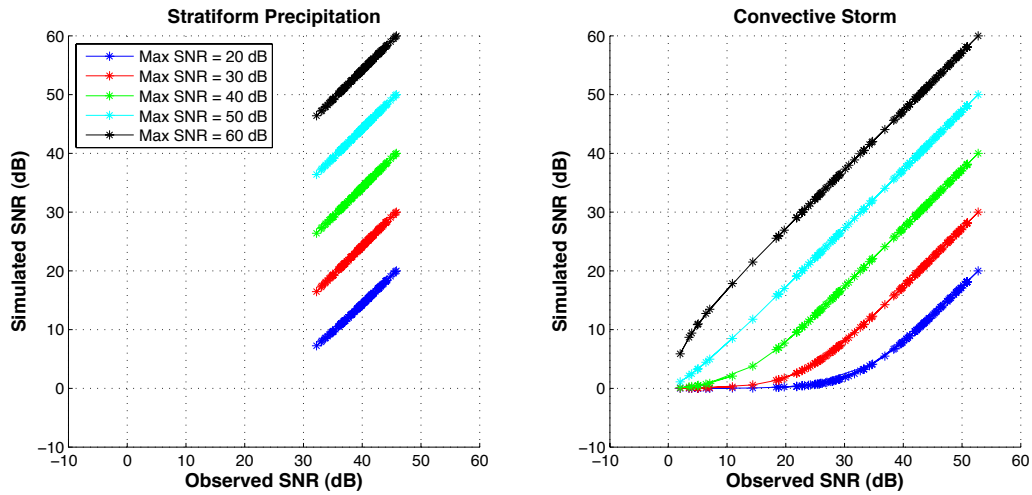

Figure 3.3: SNR of simulated weather signal versus the SNR of the observed signal for stratiform precipitation (left) and convective storm (right). The different colors correspond to the different maximum SNR listed in Table 3.1.

shift of the observed SNR; for range gates with observed SNR below a threshold, the simulated SNR are almost zero. The non linear behavior implied that when simulating weak convective storm signal, more range gates will have near zero SNR and T_{SNR} used to determine SNR weight need to be adjusted to reflect this artifact of the simulation.

3.1.1.3 Weather Simulation Result

Varying the parameters as described in Section 3.1.1.2 generated 75 different weather profiles for each of the two weather conditions and ten realizations for each weather profile were simulated to allow for statistical evaluation of the performances. Figure 3.4 shows one realization of simulated stratiform precipitation range-Doppler spectrum for different simulation parameters. As expected, the peak of the weather spectrum in each range gate is shifted, as shown in the middle left panel of Figure 3.4, when $\overline{v}$ is changed to 14m s^{-1} from the observed 6.6 m s^{-1} and $\overline{w}$ and maximum SNR are kept the same. The simulated weather signal appears stronger than the observed weather signal because the simulated signals have a higher noise power than the observed weather signals. The middle right panel shows the simulated weather range-Doppler spectrum when $\overline{w}$ is changed to 4 m s^{-1} from the observed 1.6 m s^{-1}while $\overline{v}$ and maximum SNR are kept the same. The increase in spectrum width for each range gate causes the weather signal power to spread into more frequency bins as expected. The right panel shows the simulated spectrum when $\overline{v}$ and $\overline{w}$ are kept the same and the maximum SNR is reduced from 46 dB to 30 dB. Despite the reduced SNR, the variations in signal power from gate to gate is the same as in the observed weather spectrum.

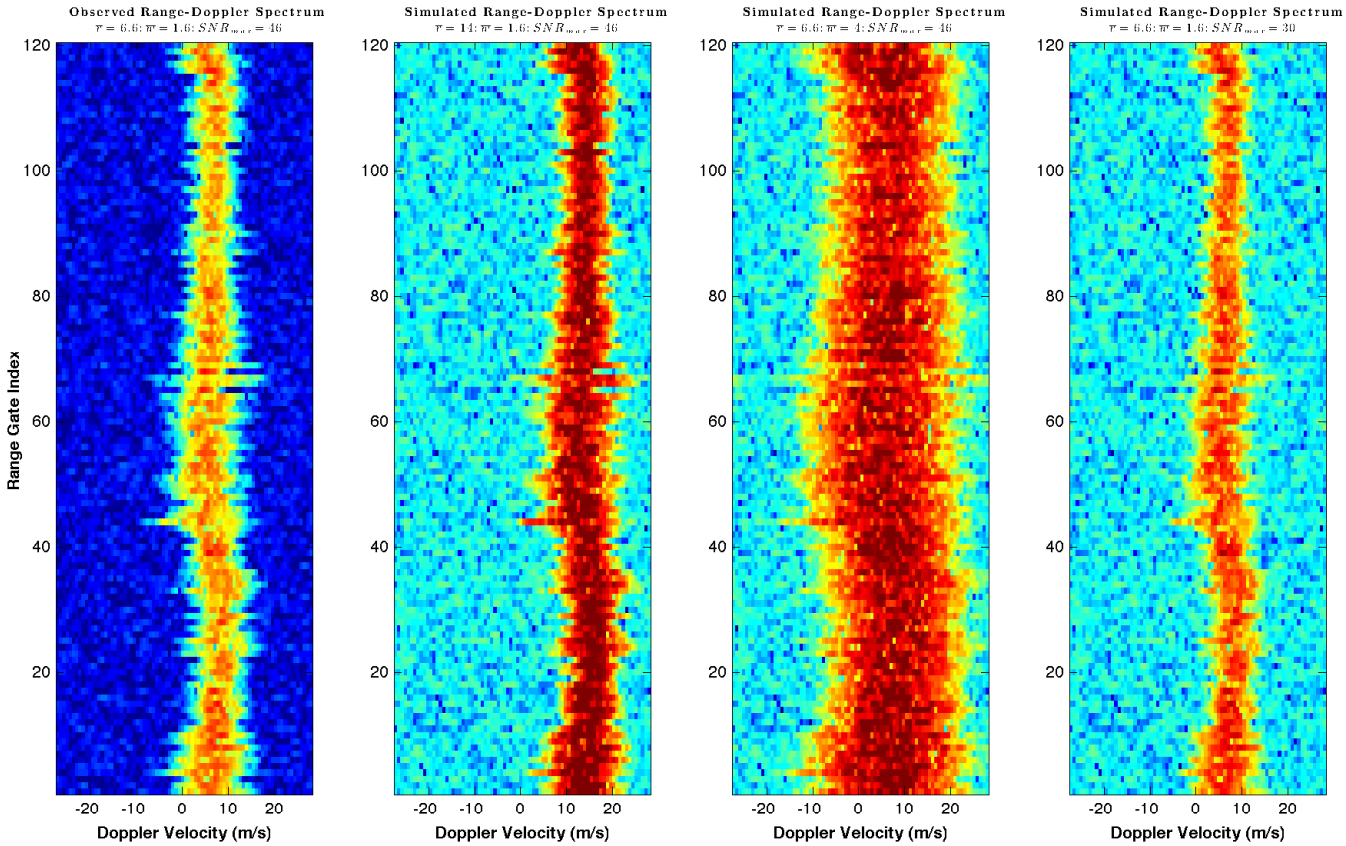

Figure 3.4: Range-Doppler spectrum of observed and simulated stratiform precipitation weather signals showing the effects of adjusting the simulation parameters. The adjustable parameters of the simulated weather signals are listed in the titles.

Since the WTC simulation process, described in Section 3.1.2, can control which range gates are contaminated, histograms of estimated velocities and spectrum widths of the simulated weather signal in those contaminated gates can be plotted to validate the weather simulator and to demonstrate that a variety of contamination situations were used to test the RDR algorithm. Figure 3.5 shows the histogram of estimated

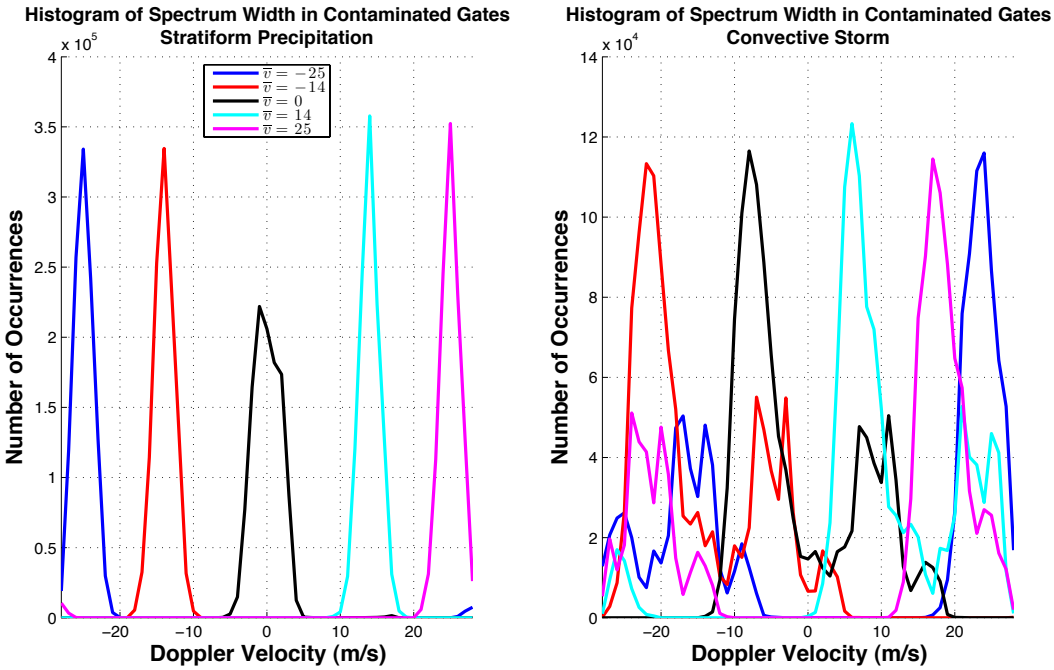

Figure 3.5: Histogram of estimated velocities in the contaminated gates for stratiform precipitation (left) and convective storm (right). The peaks in the stratiform precipitation histograms match the $\overline{v}$ used in the simulations, while the convective storm histograms are bimodal due to velocity shear.

velocities in the contaminated gates for both weather conditions. The peaks of the histograms for stratiform precipitation match the $\overline{v}$ used for the simulations because the velocity profile for stratiform precipitation is relatively constant in range as shown in Figure 3.1. The peak at 0 $\mathrm{m\,s^{-1}}$ is lower than the other peaks because the application of the GCF caused the estimated velocity to deviate from the simulated velocity, which resulted in more occurrences in the histogram bins centered around 0 $\mathrm{m\,s^{-1}}$. The histograms for convective storm are bimodal with peaks located about ± 7 $\mathrm{m\,s^{-1}}$ from the simulated $\overline{v}$. Referring to the velocity profile of convective storm in Figure 3.2, the larger peak located about -7 $\mathrm{m\,s^{-1}}$ from the simulated $\overline{v}$ results from the range gates with index between 70 to 120 and the smaller peak located about +7 $\mathrm{m\,s^{-1}}$ from the simulated $\overline{v}$ results from the range gates with index between 0 and 30.

The spectrum width distributions are shown in Figure 3.6 where the peaks correspond to the simulated $\overline{w}$ for both weather cases. Overall, a range of spectrum width from 0.5 $\mathrm{m\,s^{-1}}$ to 6 $\mathrm{m\,s^{-1}}$ for both weather conditions were generated in the simulations to test the RDR algorithm. The good match between the simulated parameters and the peaks of the histograms showed that the weather time series simulator was

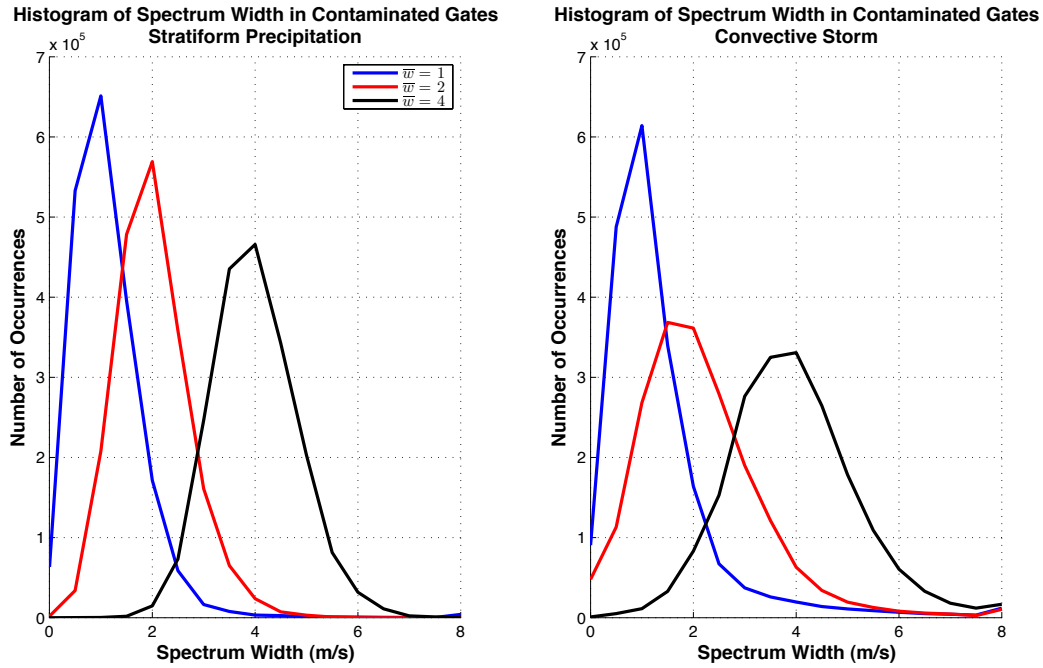

Figure 3.6: Same as Figure 3.5 except for estimated spectrum widths in the contaminated gates. The peaks correspond well to the simulated $\overline{w}$ because there are no large scale variation in velocity for both weather conditions.

functioning correctly. The histograms for simulations using different SNR_{max} will be shown in Section 3.1.2.3.

3.1.2 Wind Turbine Clutter Simulation

To control the location and degree of contamination, WTC time series were simulated using spectral shaping methods similar to the weather time series simulator used in Section 3.1.1. Ten different WTC range profiles were selected manually from data collected by KDDC in scanning mode on March 31, 2006, to cover different variations of WTC signals in range. Since the power of weather signals and the power of WTC signals vary independently in range, it is best to control the power of the simulated WTC signal through clutter-to-noise (CNR) instead of CSR. By selecting the CNR carefully and changing the index of the contaminated range gates, a good distribution of CSR was achieved. By changing the index of the contaminated range gates, different overlapping situations between weather signal and WTC signal were also simulated. Overall, 400 different range profiles were simulated to evaluated the RDR algorithm.

3.1.2.1 Observed Wind Turbine Clutter

WTC signals can have different variations in range depending on the model of the turbine, the number of turbines in the radial, and the spacing between the turbines, which makes it impractical to simulate all possible range variations of WTC signals.

As a result, ten radials were selected from data collected by KDDC in scanning mode on March 31, 2006, to function as the templates for the simulated WTC signals. Two example radials are shown in Figure 3.7 where the left panel shows a radial with

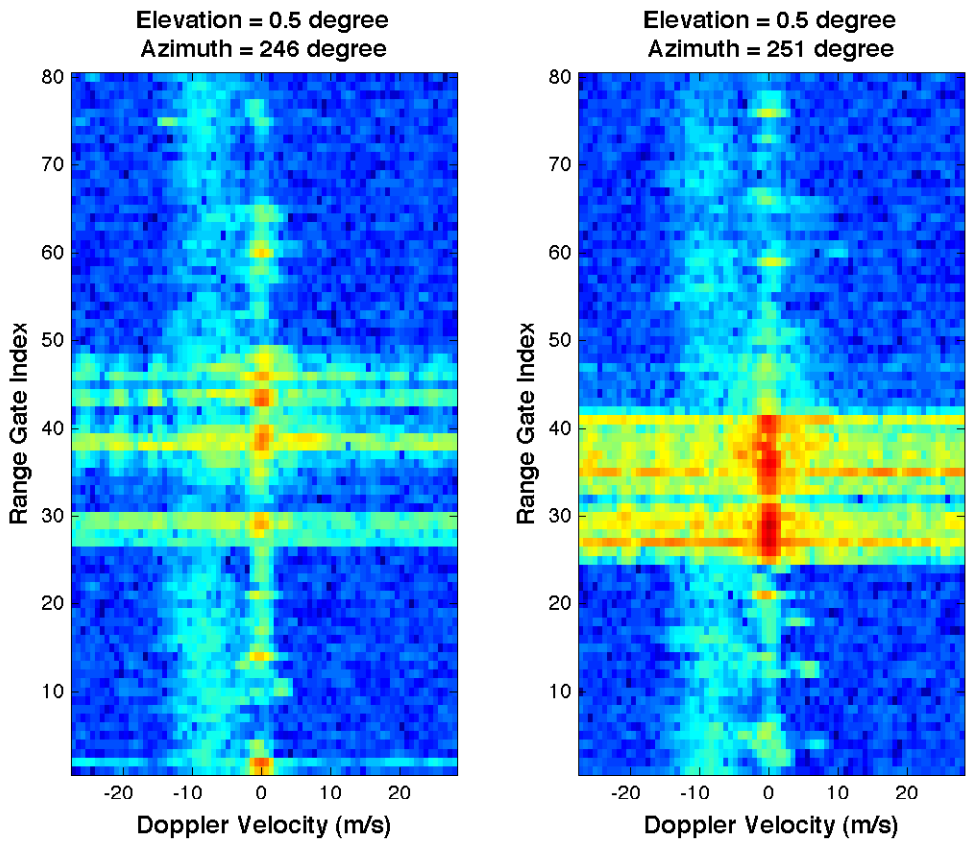

Figure 3.7: Range-Doppler spectra for two different radials showing the different range variations in WTC signals.

discontinuous WTC signal. The contaminated gates are separated from each other and most likely caused by different wind turbines. The contaminated gates in the right panel are more connected and the WTC signals are significantly stronger. Also shown in the example radials were weak weather signals located around -10 $\mathrm{m\,s^{-1}}$. To remove the weather echos in the observed data, a 30 dB SNR threshold were applied to determine which range gates had WTC signals and those range gates were used as templates for WTC simulations. For each radial, depending on the range variation of the WTC signal, one range gate immediately neighboring the range gates with WTC contamination may be manually included in the templates to preserve the natural transitions in range. For example, range gate 25 in the right panel of Figure 3.7 would be manually added to the template despite not having 30 dB SNR because it is more likely to be part of the WTC signal range variation. The noise powers in each radial were measured by averaging range gates with no signal present.

3.1.2.2 Wind Turbine Clutter Simulator

With the template of the WTC signals selected from observed data, a time series simulator using spectral shaping were developed. It was desirable to simulate WTC time series because the real data have fixed CNR which limited the range of possible CSRs. Spectral shaping based simulation was selected over model based simulations (Gallardo-Hernando et al. 2011) because the telemetry information for the observed data was not available and it was more desirable to have the simulated time series produce the same shaped Doppler spectra as the observed data to test the RDR algorithm.

The inputs to the WTC time series simulator are the Doppler spectrum and noise power for a range gate with WTC signal. Assuming the noise is white, the simulator subtract the noise power from the Doppler spectrum to produce the noiseless amplitude spectrum. Any negative spectral coefficients after the subtraction are set to zero. Random phases from a uniform distribution between $[-\pi\pi]$ are then generated for each spectral bin. The complex simulated spectrum is formed by combining the square root of the noiseless amplitude spectrum with the random phases spectral bin by spectral bin. Then an inverse Fourier transform is taken on the simulated complex spectrum to generate the time series, which can be added to the simulated weather time series to generate different testing cases for the RDR algorithm.

3.1.2.3 Combining Weather and WTC simulations

To evaluate the RDR algorithm, the simulated weather signals and WTC signals must be combined intelligently to generate the most testing cases with limited simulation parameter variations. The simulated weather signals had three adjustable simulation parameters: SNR_{max}^{sim}, $\overline{v}$ and $\overline{w}$, while the maximum CNR as was the only adjustable simulation parameter for the WTC signals. By changing the maximum CNR, the CSR of the combined signal can be varied. Combining the simulated weather signal and WTC signal was done by adding the simulated time series to a fixed noise time series. For each fixed maximum CNR, it was possible to generate more testing cases with different CSRs by changing the range gates where the WTC time series was added to the weather time series. In this work, each simulated weather signal contains 120 range range gates, while the simulated WTC signals have different number of range gates depending on the template used. For each simulated weather signal, 10 equally spaced range gates were chosen to function as the starting range gate for WTC contamination. The changing locations of the WTC signals can also test the RDR algorithms's capability to handle different spatial relationships between weather signals and WTC signals. Figure 3.8 show examples of WTC signals at different locations with different CNRs. In the left panel, the WTC contamination starts at range gate 43 and the maximum CNR is equal to 70 dB. In this testing case, there are range gates with weather signals before and after the contaminated gates, which is the ideal for the RDR algorithm. In the right panel, the contamination starts at range gate 15 and have maximum CNR equal to 90 dB. This case is more challenging for the RDR algorithm because the range gates before the contamination have weak weather signals and the clutter is much stronger than the weather signal.

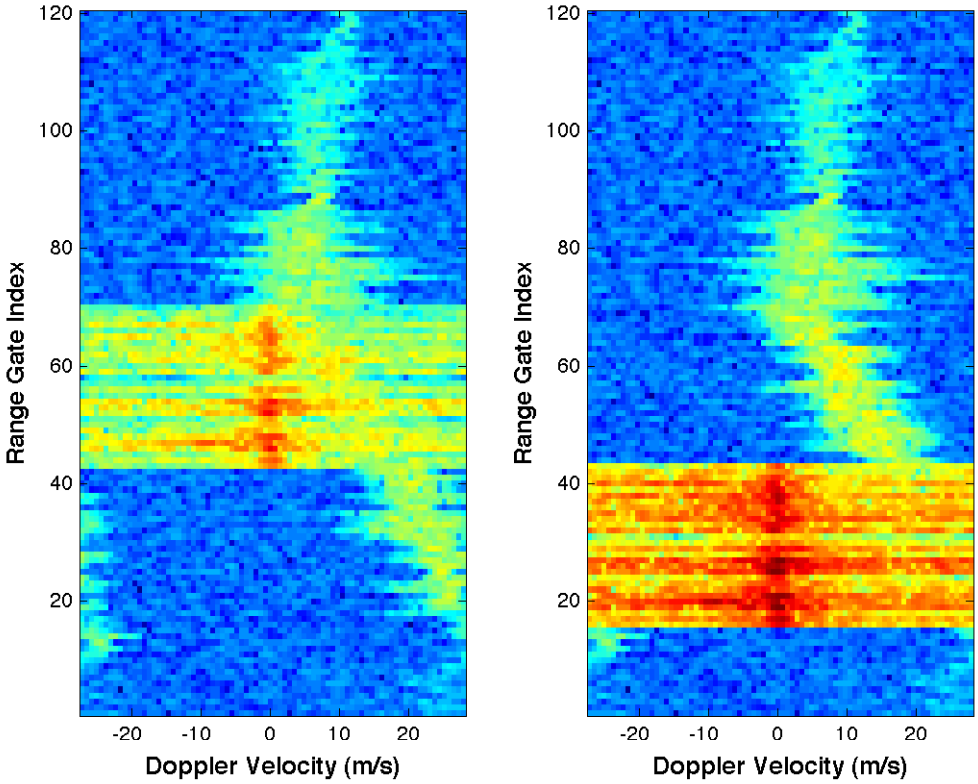

Figure 3.8: Range-Doppler spectra of simulated contaminated time series with WTC signals at different locations with different CNR. The WTC time series was simulated using the same template, and the simulated weather signal is the same for the two panels.

For each WTC template, four maximum CNR and 10 range location were used to generate 400 total unique WTC contamination cases, that combined with the 75 unique simulated weather profiles generated 30,000 testing cases with 10 realization per case for each weather conditions. In total, 600,000 range-Doppler spectrum were processed to evaluate the performance of the RDR algorithm. The SNR and CSR for each contaminated range gates in each processed range-Doppler spectrum were binned into a two-dimensional histogram, which is shown in Figure 3.9. For each

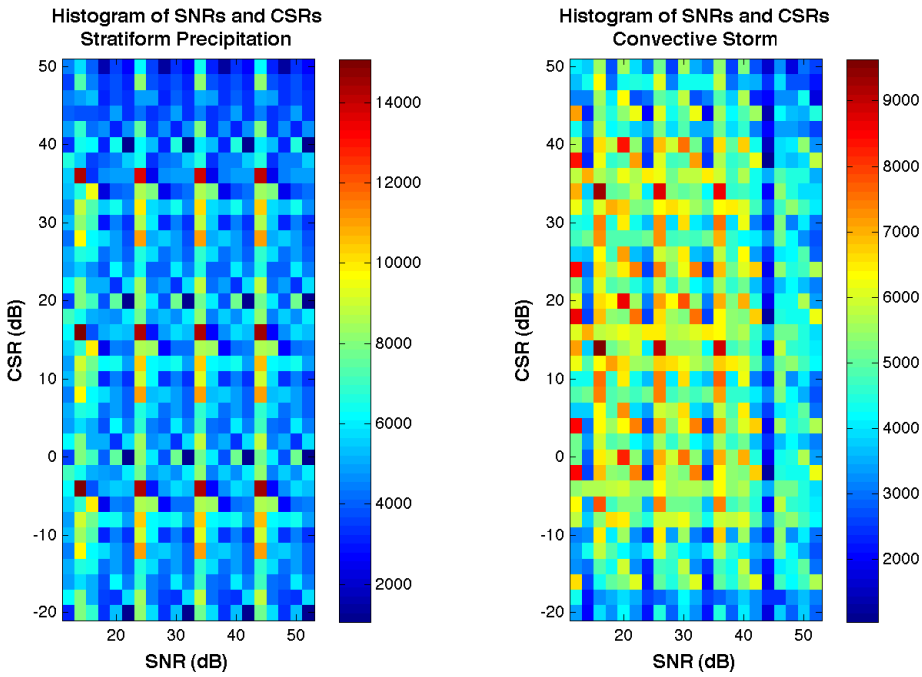

Figure 3.9: Two-dimensional histogram showing the SNR and CSR distributions of the contaminated range gates in the simulated stratiform precipitation (left) and convective storm (right) testing cases. The x-axis is the SNR of the weather signal in the range gate, the y-axis is the CSR of the WTC signal in the range gate, and the color represents how many range gates have that particular SNR and CSR combination. The bin width for both SNR and CSR is 2 dB.

SNR bin with SNR ranging from 0 dB to 60 dB and CSR bin with CSR ranging from -20 dB to 50 dB, more than 1000 contaminated gates were simulated for convective storm condition. For stratiform precipitation condition, the same hold true except no range gate with SNR below 8 dB were simulated. Despite not having equal number of testing cases for each SNR and CSR combination, the simulated signals generated enough cases to statistically evaluate the RDR algorithm for stratiform precipitation and convective storm conditions.

3.2 Simulation Results

After simulating the time series for weather and WTC signals, the parameters of the RDR algorithm was tuned and the statistical performance of the RDR was

calculated. First introduced by Hood et al. (2010), the delta biases of each spectral moment estimates were used to measure the performance of the RDR algorithm. The delta biases for the three spectral moment estimates are defined as

$$\Delta s = 10\log(\tilde{s}) - 10\log(s) \tag{3.8}$$

$$\Delta v = \tilde{v} - v \tag{3.9}$$

$$\Delta w = \tilde{w} - w \tag{3.10}$$

where Δs, Δv, and Δw are the delta biases of the power, velocity and spectrum width estimates. $\tilde{s}$, $\tilde{v}$, and $\tilde{w}$ are the power, velocity, and spectrum width estimates, respectively, after applying the RDR algorithm to a testing case, while s, v, and w are the spectral moment estimates of the simulated weather signal for the same testing case. The delta biases for each range gate were then binned according to the SNR and CSR for that range gate, and the mean delta bias, denoted by $\overline{\Delta s}$, $\overline{\Delta v}$, and $\overline{\Delta w}$ respectively, for each SNR and CSR bin were calculated. To eliminate the effects of the GCF on the performance of the RDR algorithm, range gates with weather signals having velocity with magnitude less than 1 $\mathrm{m\,s^{-1}}$ and spectrum width less than 0.5 $\mathrm{m\,s^{-1}}$ were not used in calculating the statistics of the delta biases. Range gates with simulated weather signal having spectrum width larger than 6 $\mathrm{m\,s^{-1}}$ were also excluded because weather signal with such large spectrum width rarely occur in real observations. Figure 3.10

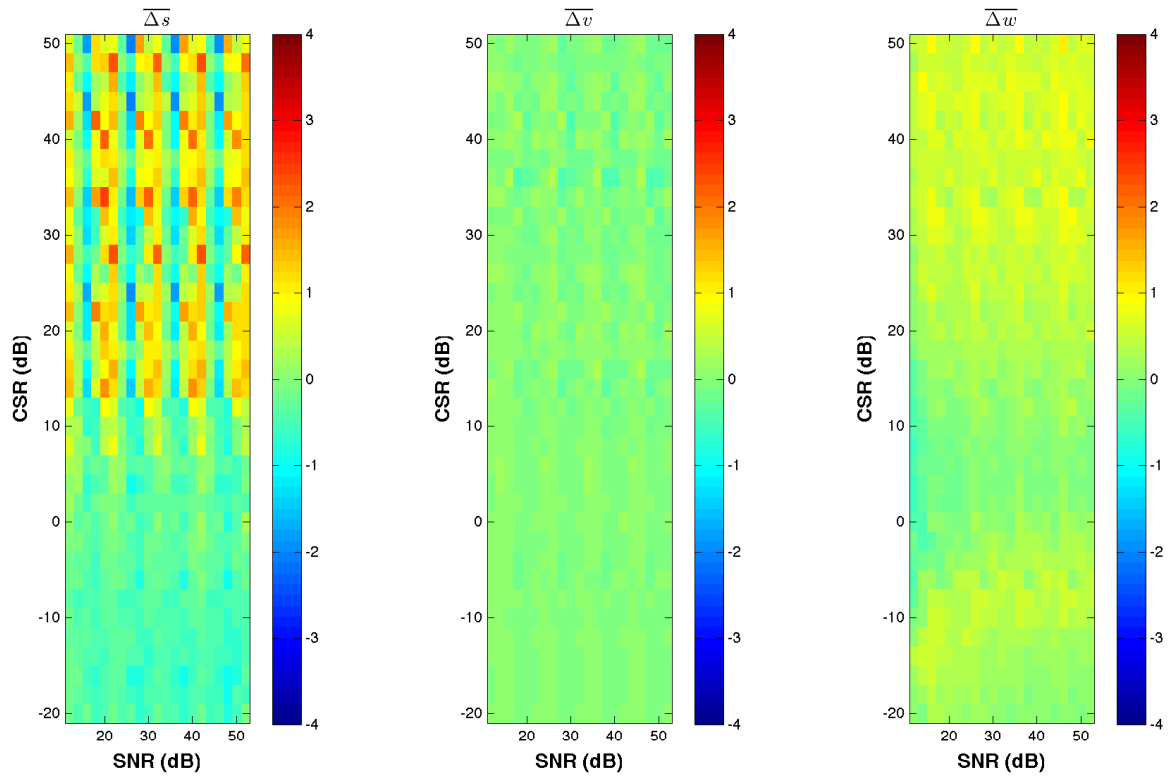

Figure 3.10: Example performance plot showing the mean delta biases for signal power (left), velocity (middle), and spectrum width (right) after applying the RDR algorithm. The x-axis is SNR, the y-axis is the CSR, and the color represents the mean delta bias for each spectral moment estimate. The SNR bins range from 12 dB to 52 dB with bin width equal to 2 dB. The CSR bins range from -20 dB to 50 dB with bin width equal to 2 dB.

shows an example performance plot for stratiform precipitation. The $\overline{\Delta v}$ and $\overline{\Delta w}$ are within ± 2 m s^{-1} for all bins, while $\overline{\Delta s}$ are slightly negative for CSR less than 10 dB, and have a periodic structure for CSR larger than 10 dB. The reason for the periodic structure is explained in Section 3.2.2.

3.2.1 Parameter Optimization

The RDR algorithm had eight parameters, which are the orders of the power, velocity, and spectrum width fit, the weather window width factor, the proximity threshold, the SNR threshold, and the threshold for CSR_{est1} and CSR_{est2}, that need to be optimized. An exhaustive search to find the optimum parameters was no practical due to the limitation of computing resources. To process all simulated testing cases would require 5.5 hours for each set of parameters, which implies a exhaustive search with three variations for each parameter would require over 4 years to complete. However, if the parameters were assumed to be independent, then a search can be performed for each parameter while the other parameters were fixed. Compared to the exhaustive search, a independent search with three variations for each parameter would only require 6 days to complete. From the description of the RDR algorithm in Section 2.4, it is clear that the parameters are not necessarily independent, but the computation convenience made it the preferred method to optimize the parameters.

Since optimizing the parameters of the RDR algorithm involves trade offs in performance for different situations, it was necessary to be able to compare the performances for different parameter sets quantitatively. The percentage of SNR and CSR bins that have $|\overline{\Delta s}|$, $|\overline{\Delta v}|$, and $|\overline{\Delta w}|$ less than their respective threshold can be used to quantify the performance images. The parameter set that gives the maximum percentage bins would be selected as the optimum parameter. In this work, the threshold for $|\overline{\Delta s}|$, $|\overline{\Delta v}|$,$|\overline{\Delta w}|$ are 2 dB, 2 m s^{-1} , and 2 m s^{-1}, respectively. The parameters were optimized in the order they appear in the RDR algorithm. The initial values for the parameters, listed in Table 3.2, were determined by visual inspection of multiple performance plots.

Table 3.2: Parameter values before optimization.

Parameter Name	**Simulated Value**
SNR Threshold	-2 dB
Proximity Threshold	13
Velocity Fit Order	2
Spectrum Width Fit Order	2
Weather Window Width Factor	2.3
Power Fit Order	2
CSR_{est1} Threshold	7 dB
CSR_{est2} Threshold	3 dB

3.2.1.1 SNR Weight Thresholds

With other parameters set to the values listed in Tabel 3.2, the SNR threshold was the first parameter to be optimized and the result is shown in Figure 3.11. The

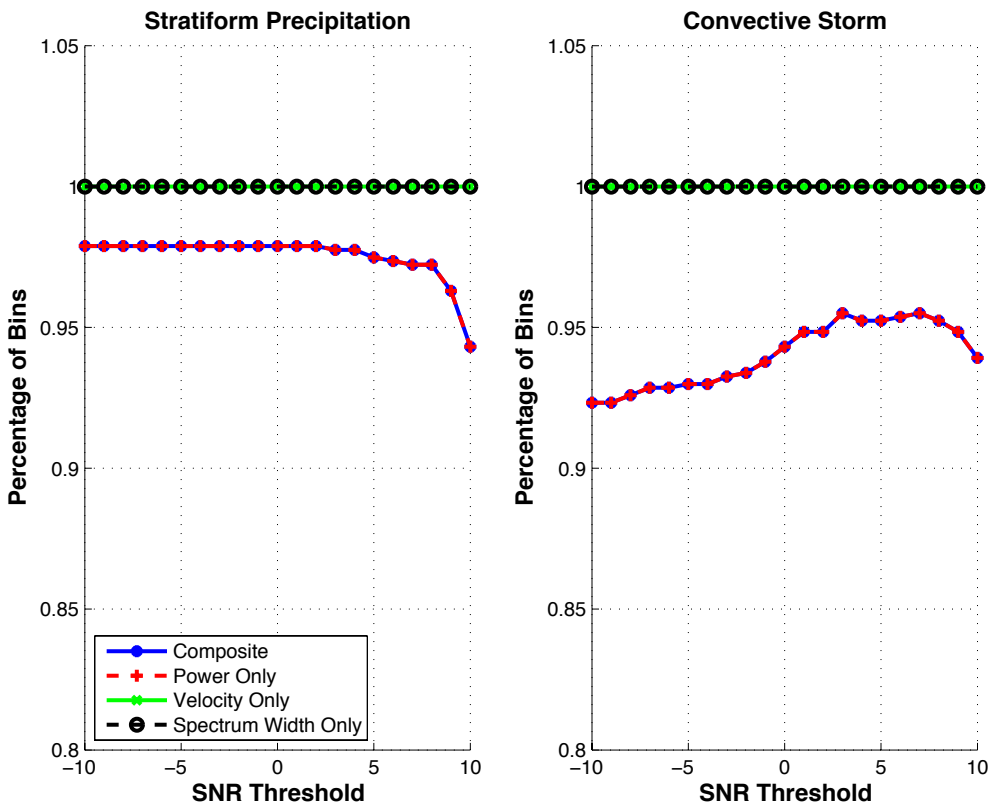

Figure 3.11: SNR threshold optimization result for stratiform precipitation (left) and convective storm (right). The x-axis is the SNR threshold and the y-axis is the percentage of bins that have delta biases below the threshold. The SNR threshold is changed from -10 dB to 10 dB in 1 dB steps.

red, green, and black curves shows the percentage of bins that have $|\overline{\Delta s}|$, $|\overline{\Delta v}|$, and $|\overline{\Delta w}|$ less than the thresholds individually while the blue curve shows when delta biases for all three spectral moments are less than the thresholds. For stratiform precipitation, Figure 3.11 shows that $|\overline{\Delta v}|$ and $\overline{\Delta w}|$ are less than 2 $\mathrm{m\,s^{-1}}$ for all bins and all SNR threshold values. The limiting factor on the performance is the delta bias for signal power estimates. The composite performance for stratiform precipitation did not degrade as the SNR threshold become negative because all range gates in the simulated stratiform precipitation weather profiles had SNR above 0 dB and no range gate containing noise signal only received non-zero weighting despite the SNR threshold being negative. When the SNR threshold become large, gates with significant weather signals received zero weighting and the performance for stratiform precipitation condition degraded.

Similarly, the performance curves for convective storm weather shows that the bias for signal power estimates determines the overall performance of the algorithm.

Then the SNR threshold is decreased below 0 dB, the performance of the algorithm degraded because range gates with noise signal were allowed to contribute to the velocity and spectrum width fit. The non-linear scaling of the SNR, shown in Figure 3.3, caused more range gates in the simulated weather signal to have near zero SNR, which lead to negative SNR estimates after the GCF is applied. The presence of negative SNR estimates causes the performance of the algorithm for SNR threshold between -10 to -1 dB continue decreasing because more range gates with noise signal only were included in the fits. When the SNR threshold is above 7 dB, the performances for stratiform precipitation and convective storm both decreased because range gates with weather signal were excluded from the fits. Based on the composite performance curve for both weather cases, 3 dB was selected as the optimum SNR threshold for the reminder of the study.

3.2.1.2 Proximity Threshold

The second set of weights used in the low-order polynomial fits for velocity and spectrum width was based on the proximity of a non-contaminated gate to the closest contaminated gates. Varying the proximity threshold changes the maximum number of gates that could receive non-zero weighting and Figure 3.12 shows the performance

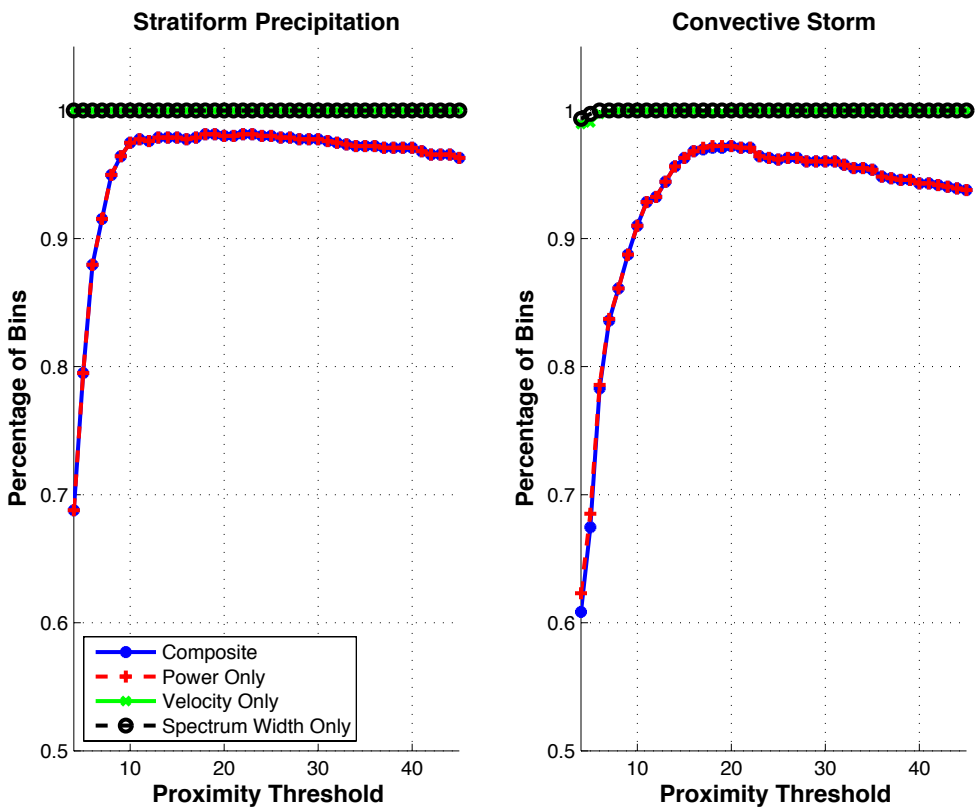

Figure 3.12: Same as Figure 3.11 except the x-axis is the proximity threshold. The proximity threshold is changed from 4 gates to 45 gates in increment of 1 gate.

as a function of proximity threshold. Other parameters were set to the values in

Table 3.2. For both weather conditions, the delta biases of the power estimates after applying the RDR algorithm limits the overall performance of the RDR algorithm. The magnitude of mean delta bias for both velocity and spectrum width after processing is below 2 $\mathrm{m\,s^{-1}}$ threshold for all SNR and CSR bins as long as the proximity threshold is larger than 10. When the proximity threshold is small, the performance of the RDR algorithm declined sharply because the velocity and spectrum width fit did not capture the local trend robustly, which is caused by not having enough spectral moment estimates with non-zero weight to use in the fits. The performance for power also decreased when the proximity threshold is large because information from range gates that are far away from the contaminated gates were less useful in predicting the weather power in the contaminated gates. As the proximity threshold is increased, the decline in performance is slower for stratiform precipitation than for convective storm because the decorrelation distance of weather signal power is larger for stratiform precipitation.

The proximity threshold that gave the best performance for stratiform precipitation and convective storm did not match exactly, but both had peak located between 15 and 25 range gates, and the proximity threshold was set to 20 gates for the remainder of the study.

3.2.1.3 Velocity Fit Order

After determining the parameters to set the weights for the velocity and spectrum width fits, the next parameter to be optimized was the velocity fit order. Figure 3.13 shows the performance of the RDR algorithm as a function of the velocity fit order. For stratiform precipitation, the performance curve suggests that the performance does not depend on the velocity fit order for the lowest orders. The extremely small variations in performance could be caused by statistical fluctuations. For convective storm, the performance of the algorithm shows a drop off when the velocity fit is higher than third order. The reason for the drop off is that when there are a large number of consecutive gates that are contaminated, a high order fit introduces artificial velocity variation in the contaminated gates. The optimum velocity fit order is selected to be second order because previous parameters were optimized using second order velocity fits and the differences in performance between second order and first or third order are minimal.

3.2.1.4 Spectrum Width Fit Order

The spectrum width fit was varied from first order to fifth order in an attempt to find the optimum fit order. Figure 3.14 shows the performance of the RDR algorithm as a function of the spectrum width fit order. Similar to velocity fit order, the differences in performance for stratiform precipitation are minimal and may be caused by statistical fluctuations. For convective storm, there are slightly improvements in performance for fourth and fifth order fits, but the improvements are not significant enough to justify changing the optimum spectrum width fit order from second order to fifth order.

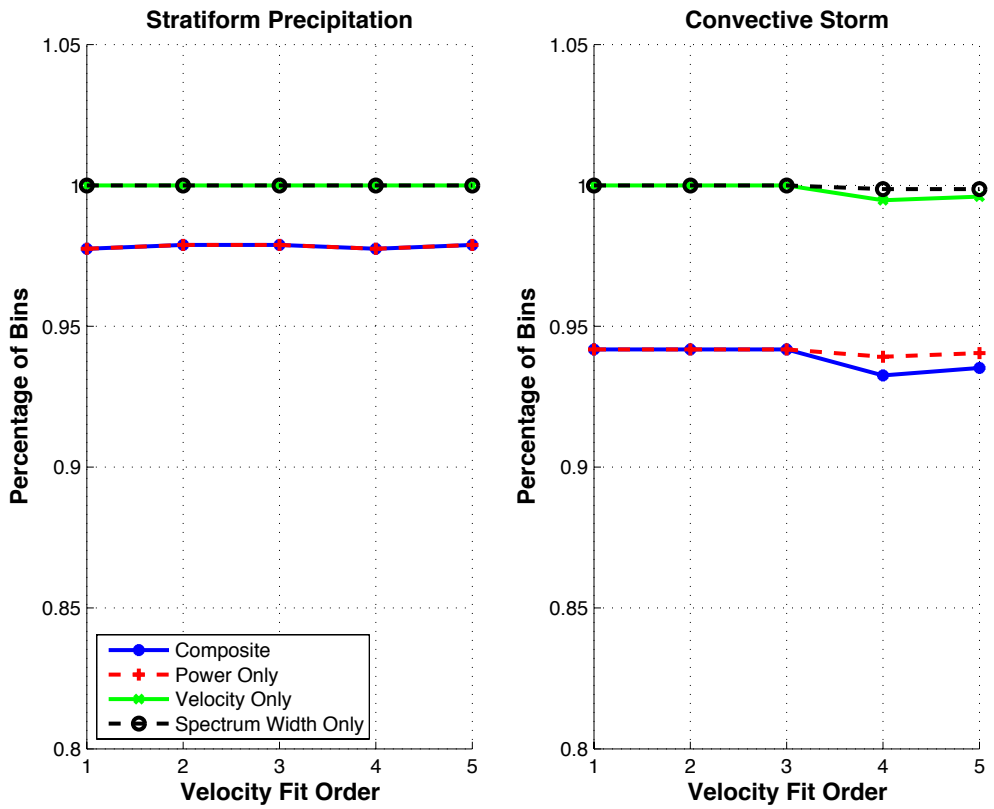

Figure 3.13: Same as Figure 3.11 except the x-axis is the velocity fit order. The velocity fit is varied from first order to fifth order.

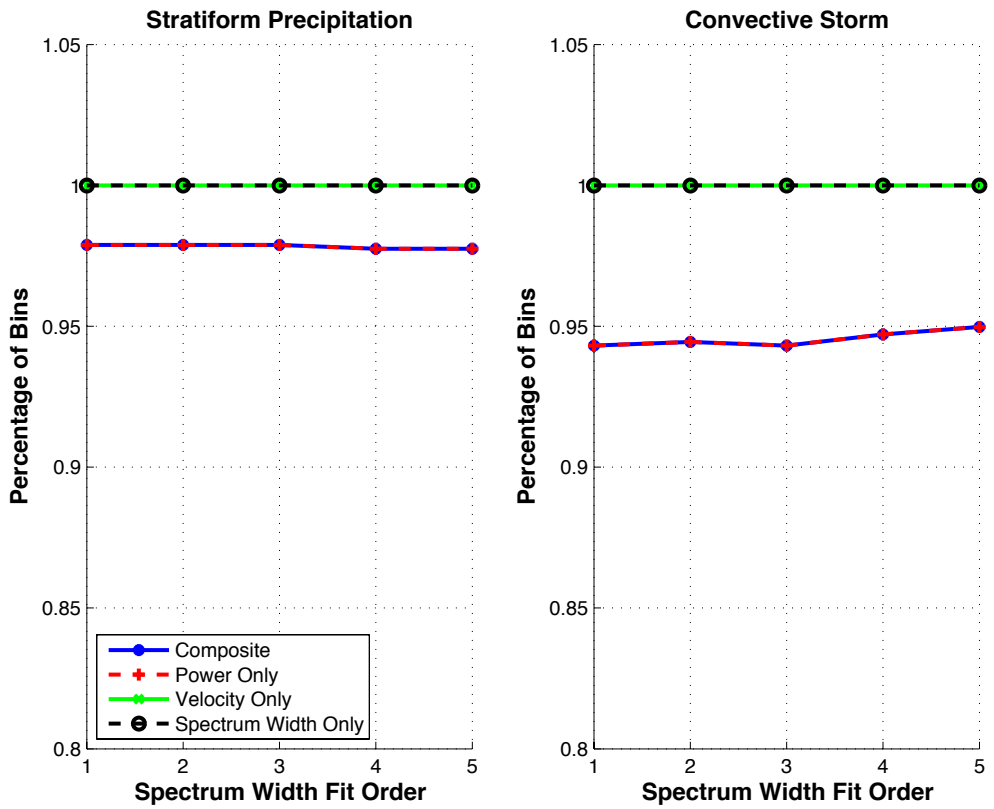

Figure 3.14: Same as Figure 3.11 except the x-axis is the spectrum width fit order. The spectrum width order is varied from first order to fifth order.

3.2.1.5 Weather Window Width Factor

The weather window width factor is the last parameter that controls the estimation of the weather window. It limits the maximum spectrum width bias according to

$$Bias_{max}(\sigma_v) = \left(\frac{K}{\sqrt{3}} - 1\right)\sigma_v \tag{3.11}$$

where K is the weather window width factor and σ_v is the spectrum width estimate. Equation (3.11) was derived by assuming the fitted spectrum width is equal to the spectrum width of the uncontaminated weather signal and and spectral coefficients inside the weather window are constant. The optimum K cannot be set to $\sqrt{3}$ because the fitted spectrum width rarely equal the spectrum width of the uncontaminated weather signal and the spectral coefficients inside the weather window are never constant. However, Equation (3.11) does imply that the optimum K should not be extremely large or small.

The simulation results are shown in Figure 3.15 with several interesting features. For both stratiform precipitation and convective storm, the spectrum width only per-

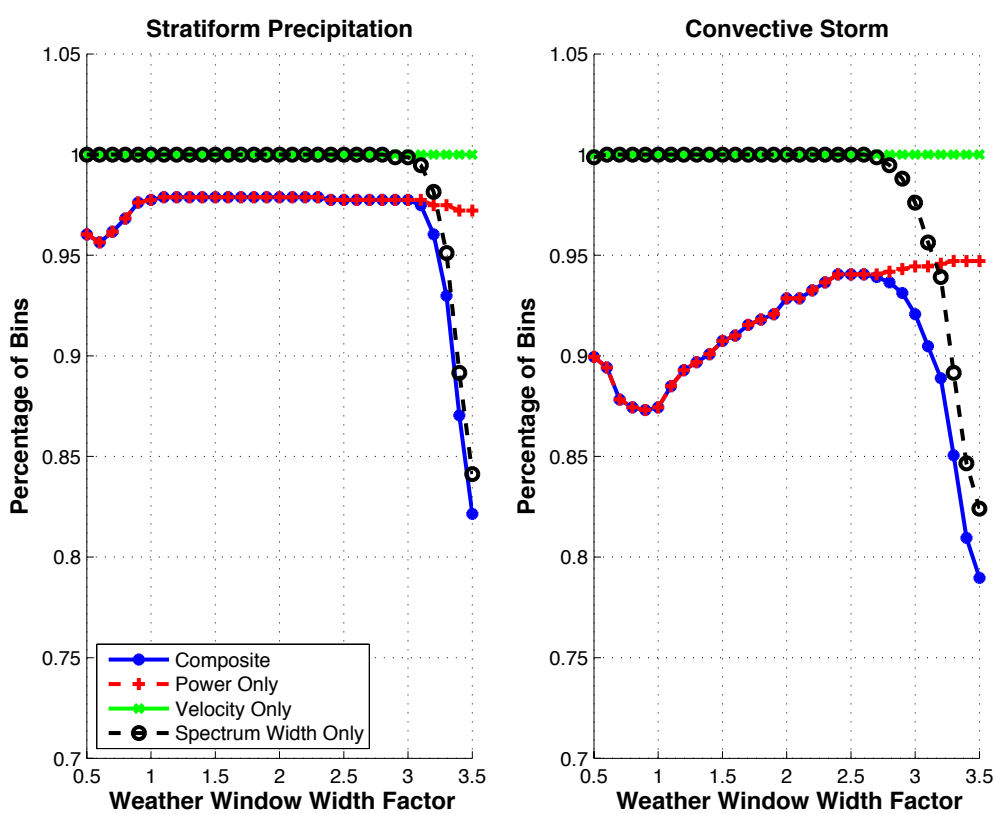

Figure 3.15: Same as Figure 3.11 except the x-axis is K. K is increased from 0.5 to 3.5 in 0.1 increments.

formance curve decreases sharply for large K values, which is expected according to Equation (3.11). The velocity only performances are unaffected because the weather window is symmetric around the fitted velocity and increasing K should not affect

the velocity estimates if the weather window has captured the majority of the weather spectral coefficients. The power only performance for stratiform precipitation is almost constant once K is larger than 1, and the performance for convective storm is continuously increasing for K ranging from 1 to 3.5. The reason for the continuous increase in power performance is that for large K, the majority of the spectrum is included in the weather window. For low CSRs, using the majority of the spectrum to estimate the weather signal power is better because the likelihood of the weather window missing the weather signal is reduced. For high CSRs, the weather signal power estimates are based on a low-order polynomial fit rather than the weather window, so a larger weather window containing more WTC power does not negatively impact the performance. The slight increase in performance for K equals to 0.5 is explained by the fact that an extremely narrow weather window will significantly underestimate the weather power, which causes CSR_{est2} to be artificially increased. Larger CSR_{est2} leads to the fitted power being used as the weather signal power estimate, which are more accurate than the power estimates based on the narrow weather window.

Based on the performance curves, the optimum K is 2.5. Since the performance difference between 2.3 and 2.5 are small and 2.3 was used in previous optimizations, it is selected as the optimum value for the rest of the optimization.

3.2.1.6 Power Fit Order

As discussed in Section 2.4.2, the WTC power contained in the weather window will bias the weather signal power estimates, and the degree of biases depends on the CSR. For high CSRs, the biases caused by the WTC power inside the weather window is significant and a weighted low-order polynomial fit using non-contaminated weather signal power become a better estimator for the weather signal power in the contaminated gates. The performance of the RDR algorithm for different power fit orders are plotted in Figure 3.16. Both stratiform precipitation and convective storm show the same trend where the performances are better for second or third order fit and are lower for first, fourth, and fifth order fits. The higher order fits performed poorly for both weather cases because the extra degrees of freedom allowed the fitted power to not follow the local trend of the weather signal power when a large number of consecutive range gates were contaminated. The first order fits could not capture the local trend in weather signal power, especially for convective storm. Based on Figure 3.16, the optimum power fit order was set to two.

3.2.1.7 CSR Estimator Thresholds

The independent search optimization result for CSR_{est1} threshold is shown in Figure 3.17. The decision logic for whether to base the weather signal power estimate on the weather window or the low-order fit is shown in Table 3.3. Based on the decision logic, the weather signal power estimate is determined by the low-order fit for all CSRs when a low CSR_{est1} threshold is used. In Figure 3.17, the performances forCSR_{est1} threshold equals -10 dB approximate the performances when the fit is always used, and the performances are good but not the best. When a high threshold

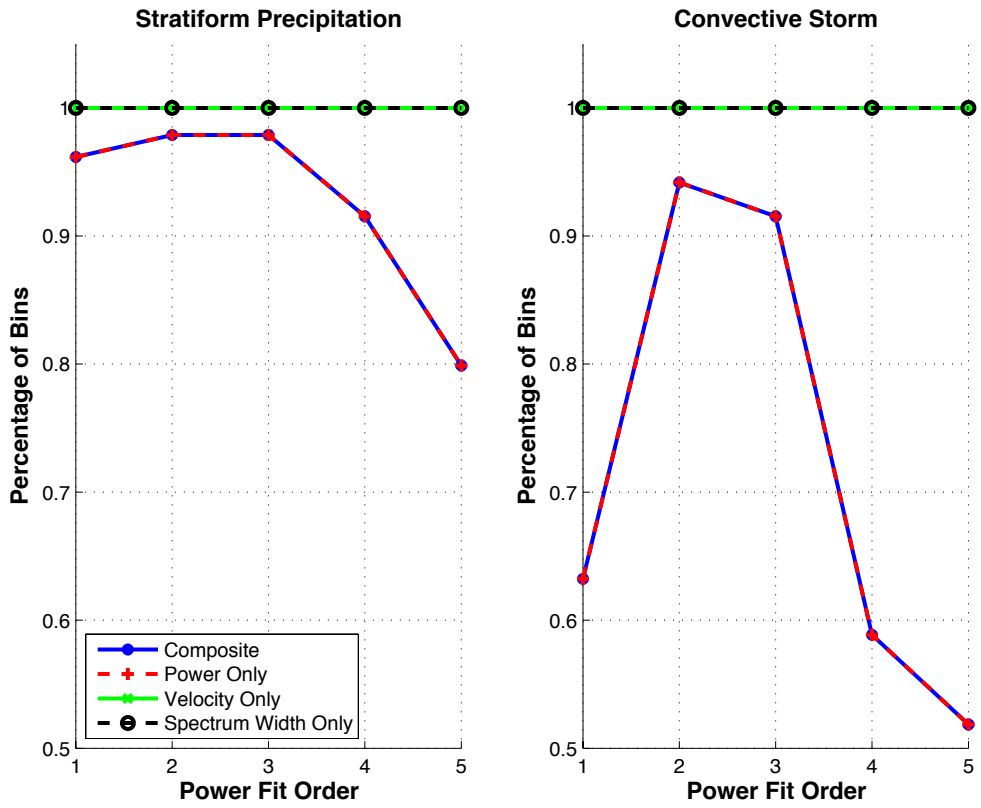

Figure 3.16: Same as Figure 3.11 except the x-axis is the power fit order. The power fit order is varied from first order to fifth order.

Table 3.3: Decision logic for weather signal power estimate.

	$CSR_{est1} <$ **Threshold**	$CSR_{est1} \geq$ **Threshold**
$CSR_{est2} <$ **Threshold**	Weather Window	Low-Order Fit
$CSR_{est2} \geq$ **Threshold**	Low-Order Fit	Low-Order Fit

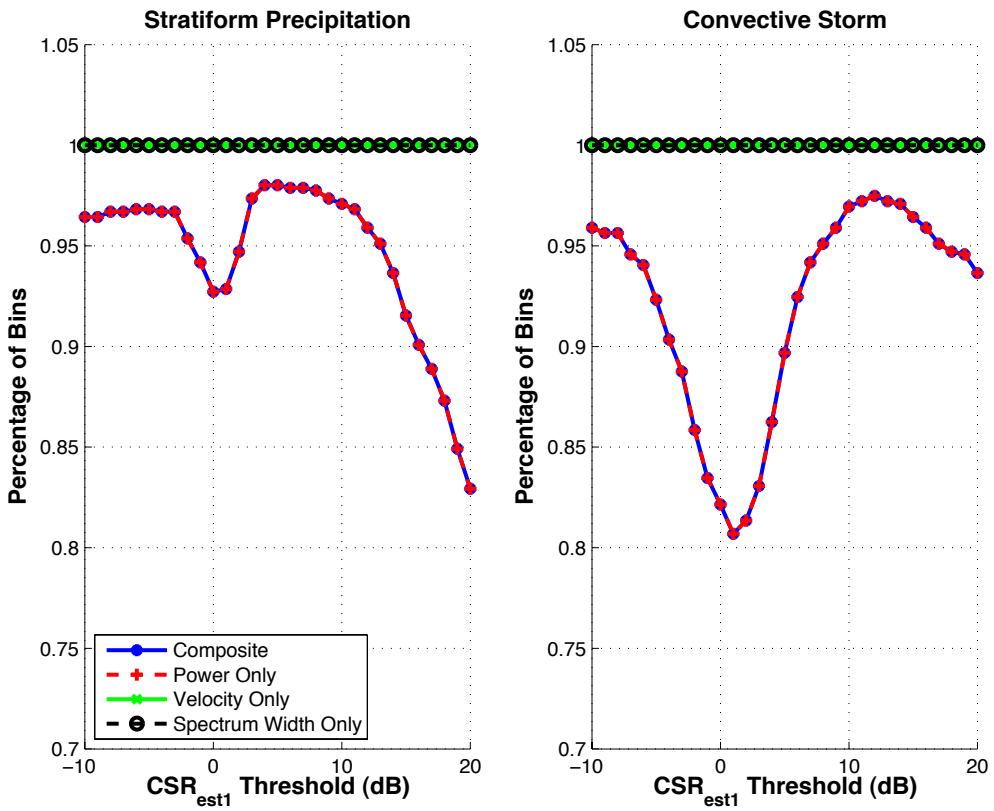

Figure 3.17: Same as Figure 3.11 except the x-axis is the CSR_{est1} threshold. CSR_{est1} threshold is varied from -10 dB to 20 dB in 1 dB increment.

for CSR_{est1} is used, the decision to base the weather signal power estimate on the weather window or the low-order fit is entirely determined by the CSR_{est2} threshold, but as discussed in Section 2.4.2, only using CSR_{est2} to make the decision was not ideal because CSR_{est2} had large variances. The decline in performance for both weather cases for high CSR_{est1} thresholds matched the expectation. Since CSR_{est1} asymptotically approaches 0 dB when the true CSR is smaller than 0 dB, having a threshold at 0 dB essentially reduces the decision to use the weather window or the low-order fit for weather signal power estimate to whether the fit overestimate or underestimate the weather signal power. If the fit overestimate the weather signal power, CSR_{est1} would be less than 0 dB and the weather window would be used to determine the weather signal power estimate, and if the fit underestimate the weather signal power estimate, CSR_{est1} would be larger than 0 dB and the fit would be used to determine the weather signal power estimate. By using the fit only when it underestimate the weather signal power, the performance for both weather cases reaches a minimum as shown in Figure 3.17. Considering both weather cases, the optimum CSR_{est1} threshold according to Figure 3.17 is around 10 dB.

The performance of the RDR algorithm as a function of CSR_{est2} threshold is plotted in Figure 3.18. Based on Table 3.3, small CSR_{est2} threshold implies the low-

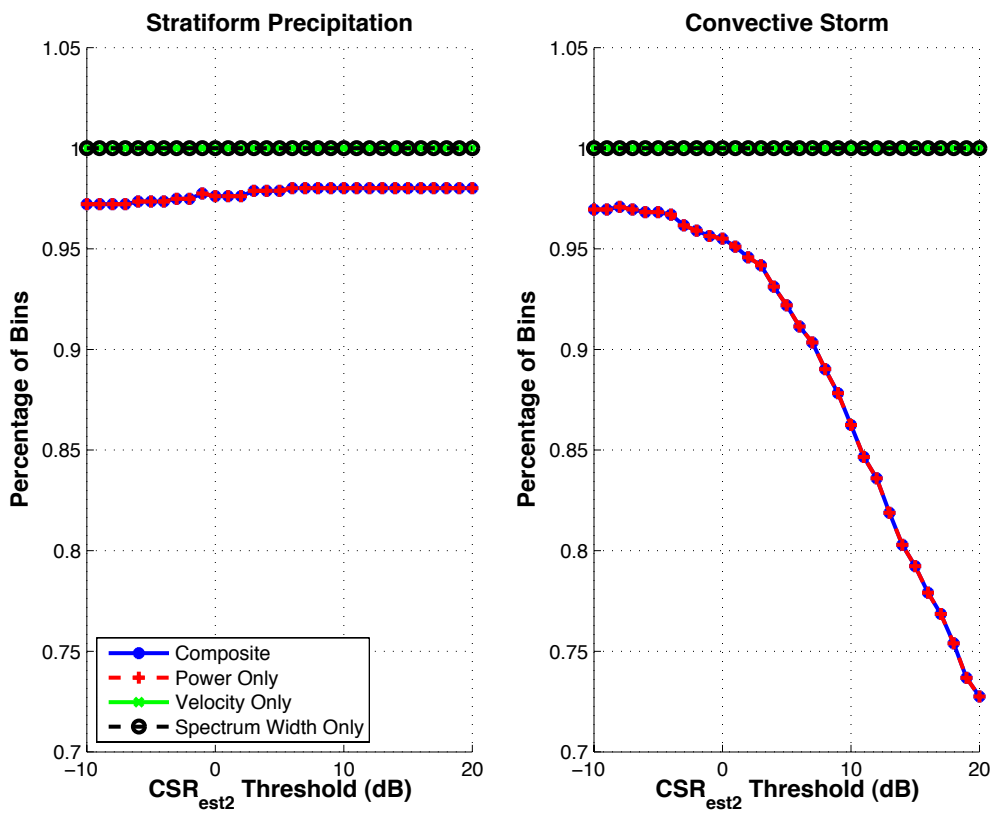

Figure 3.18: Same as Figure 3.17 except the x-axis is the CSR_{est2} threshold.

order fit is used to determine the weather signal power estimate for all CSRs regardless what threshold is set for CSR_{est1}. When CSR_{est2} threshold is raised, the performance

for convective storm falls off rapidly because CSR_{est1} is used solely to determine the weather signal power estimates. For low CSRs, using only CSR_{est1} causes the fit to be used only when it is underestimating the weather signal power, resulting in large delta biases. For stratiform precipitation, the performance improved slightly as the CSR_{est2} threshold is increased. The reason for the contrasting trend is that CSR_{est1} has lower variance for stratiform precipitation, and the problem of using the fit only when it underestimates the weather signal power is mitigated somewhat by CSR_{est1} threshold being 7 dB for the CSR_{est2} optimization runs. According to Figure 3.18, the optimum CSR_{est2} threshold is around -2 dB.

Because the CSR_{est1} and CSR_{est2} thresholds are used together to decide whether the weather window or the fit is used to determine the weather signal power estimates, a two-dimensional search is performed to serve as a confirmation for the independent search results. Figure 3.19 shows the composite results for both weather

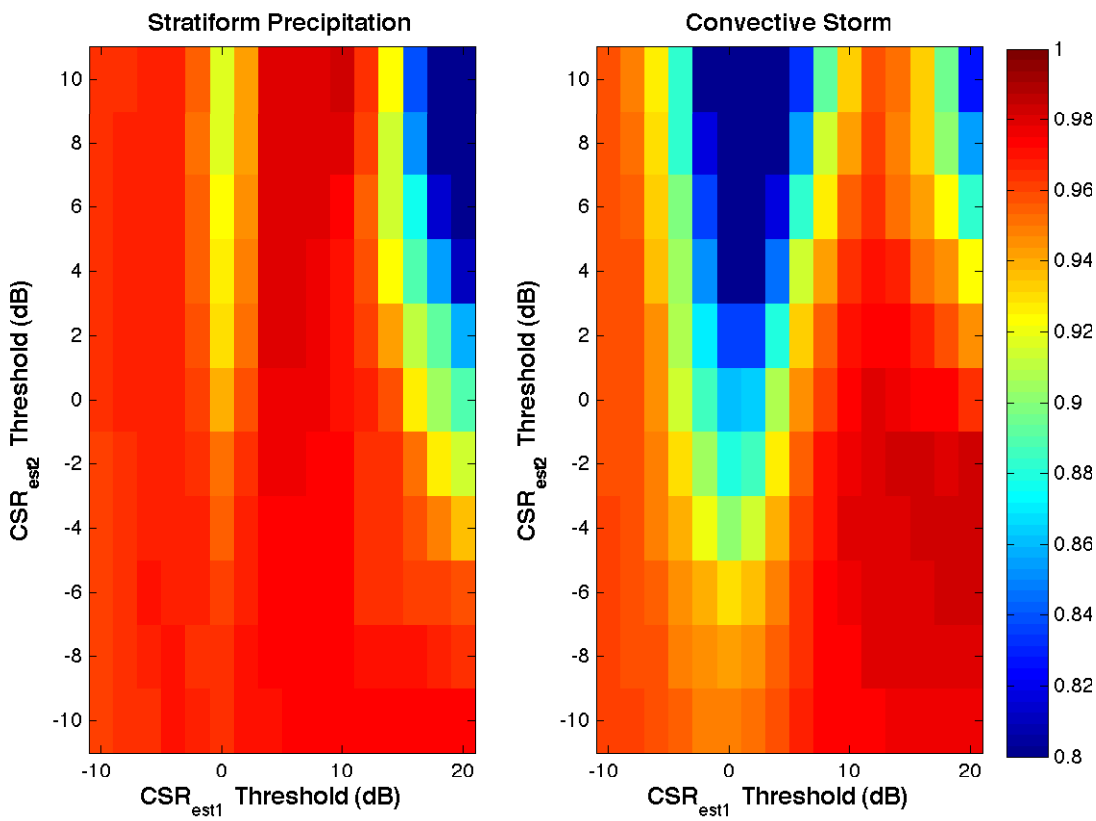

Figure 3.19: Performance of the RDR algorithm as a function of CSR_{est1} and CSR_{est2} thresholds for stratiform precipitation (left) and convective storm (right). The x-axis is CSR_{est1} threshold, which is varied from -10 dB to 20 dB in 2 dB increments. The y-axis is the CSR_{est2} threshold, which is varied from -10 dB to 10 dB in 2 dB increments. The color for each threshold pair represent the percentage of bins having acceptable mean delta bias for all three spectral moments.

cases. The minima in performance always occur whenCSR_{est1} threshold is around 0 dB for any fixed CSR_{est2} threshold, implying the performance curves plotted in

Figure 3.17 is typical. For convective storm, the same trend as in Figure 3.18 occurs for each fixed CSR_{est1} threshold. However, the trend in Figure 3.18 for stratiform precipitation does not hold for all CSR_{est1} thresholds. For large CSR_{est1} thresholds, the stratiform precipitation performance as a function of CSR_{est2} threshold follows the same trend as the convective storm performance where the performance decreases as CSR_{est2} threshold increases. To find the optimum threshold using Figure 3.19, the performances for both weather cases is averaged for each threshold pair, and optimum thresholds are 10 dB and -4 dB for CSR_{est1} and CSR_{est2}, respectively. The two-dimensional search results confirmed the optimum thresholds determined using independent search, which provides more confidence in other optimum parameters found using independent search. The final optimum parameter values are listed in Table 3.4 and the performance of the RDR algorithm with the optimum parameters are presented in the next section.

Table 3.4: Parameter values after optimization.

Parameter Name	**Simulated Value**
SNR Threshold	3 dB
Proximity Threshold	20
Velocity Fit Order	2
Spectrum Width Fit Order	2
Weather Window Width Factor	2.3
Power Fit Order	2
CSR_{est1} Threshold	10 dB
CSR_{est2} Threshold	-4 dB

3.2.2 RDR Algorithm Performance Assessment

After determining the optimum parameter values, the RDR algorithm with the optimum parameters was applied to all realizations of simulated time series, and the performances for stratiform precipitation and convective storm are shown below.

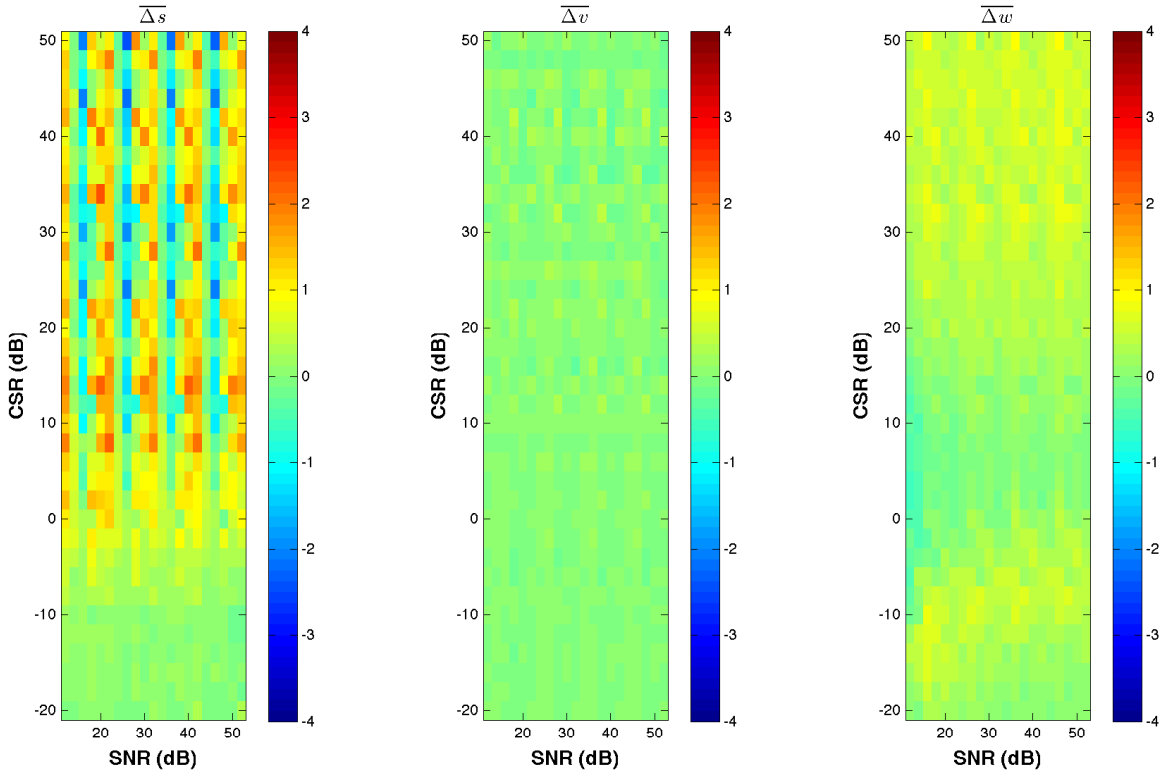

Figure 3.20: Performance of the RDR algorithm for stratiform precipitation using optimum parameters. The mean delta bias for weather signal power (left), velocity (middle), and spectrum width (right) are plotted as a function of SNR and CSR of the contaminated gates.

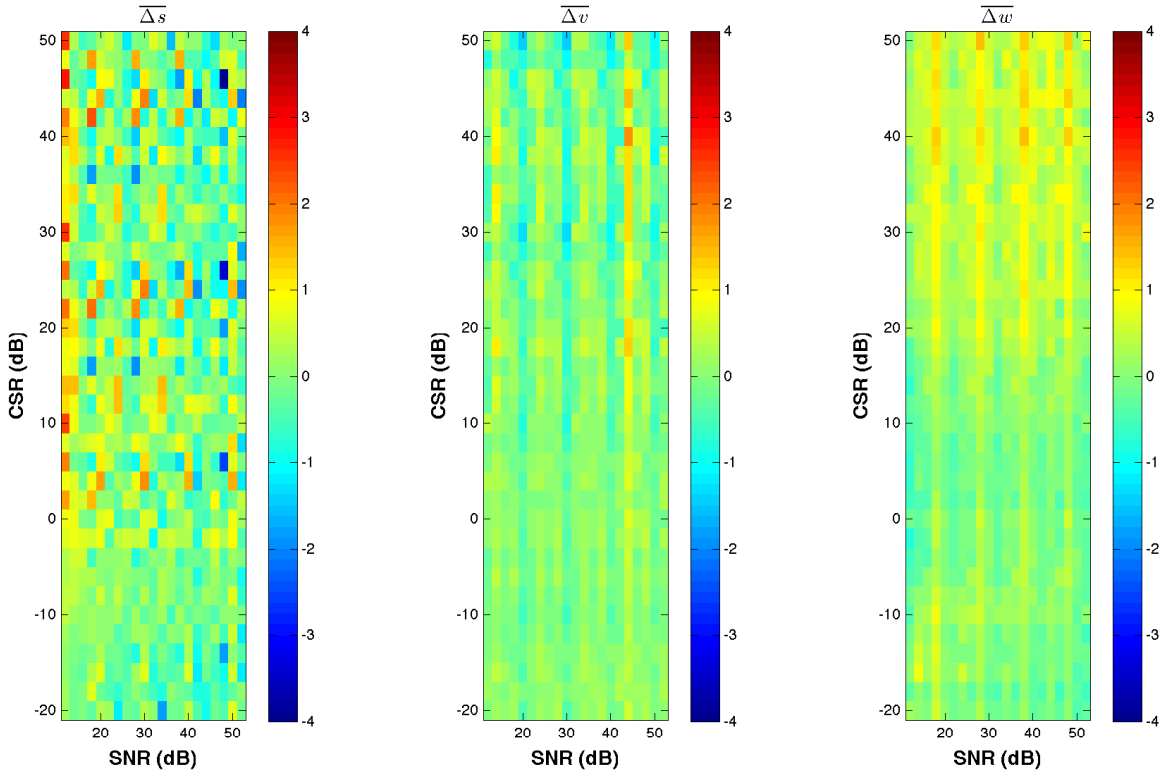

Figure 3.21: Same as Figure 3.20 except for convective storm.

For both stratiform precipitation and convective storm, $|\overline{\Delta v}|$ and $|\overline{\Delta v}|$ are less than 2 m s^{-1} for all SNRs and CSRs. For convective storm, $|\overline{\Delta s}|$ is less than 2 dB for 98.3% of the bins with maximum $\overline{\Delta s}$ being 2.75 dB and minimum $\overline{\Delta s}$ being -3.92 dB. For stratiform precipitation, applying the RDR algorithm to stratiform precipitation reduced$\overline{\Delta s}$ to less than 2 dB for 97.5% of the bins, and the maximum $\overline{\Delta s}$ is 2.30 dB and the minimum of -2.42 dB. The extreme values of $\overline{\Delta s}$ indicate that the RDR algorithm did not fail completely for the SNR and CSR combinations that have $|\overline{\Delta s}|$ over 2 dB.

Observing the $|\overline{\Delta s}|$ plot for stratiform precipitation in Figure 3.20, there is a periodic occurrence of positive and negative $\overline{\Delta s}$ as a function of SNR for CSR greater than 0 dB. For high CSR, the low-order polynomial fit is used to determine the weather signal power estimate after applying the RDR algorithm. Since the weather signal power have natural variations in range, the fit would overestimate the weather signal power for a range gate if that gate have lower SNR than its neighboring gates. If the range gate has a higher SNR than its neighboring gates, then the fit would underestimate the weather signal power. This behavior of the fit generates a patter of positive and negative Δs for each set of simulated weather signal, and the pattern is repeated because five set of weather signals with different maximum SNR were simulated.

The performances of the RDR algorithm shown in Figure 3.20 and 3.21 contain all simulated weather signals except the cases where the simulated weather signal have a spectrum width less than 0.5 m s^{-1} and velocity between ± 1 m s^{-1}, and those cases were removed to prevent the biases introduced by the GCF from being included in the performance evaluations of the RDR algorithm. To further evaluate the RDR algorithm, performances for different velocity and spectrum width groups are shown next. Figure 3.22 show the performance of the RDR algorithm for stratiform precipitation with small velocities. The performance is worse than the performance when all velocities are included, especially for cases with CSR between 10 to 20 dB. The hub component of the WTC contamination located near zero Doppler causes CSR_{est2} to be negatively biased, which leads to more cases with medium CSR to using the weather window to determine the weather signal power estimate. Since the weather window for a weather signal with near zero velocity include the hub contamination, the power estimates after applying the RDR is more positively biased. Figure 3.23 and 3.24 shows the performance for stratiform precipitation with medium and high velocities, respectively. Since the weather signals are located farther away from the hub component of the WTC contamination, the performances matches the overall performance much better. The same trend holds for convective storm as well.

The performances of the RDR algorithm for weather signals with different spectrum width is shown next. Observing Figure 3.25 and 3.26, the RDR performs well for convective storms with spectrum width less than 4 m s^{-1}. For weather signals with larger spectrum width, there are is a large increase in $\overline{\Delta s}$ for CSR greater than 0 dB, which can be seen in Figure 3.27. The same increase in delta bias for weather signal power estimate also occurs for stratiform precipitation. One reason for the increase in delta bias is the small number of range gates with spectrum width larger than 4 m s^{-1}. The histogram of the spectrum width distribution, shown in Figure 3.6,

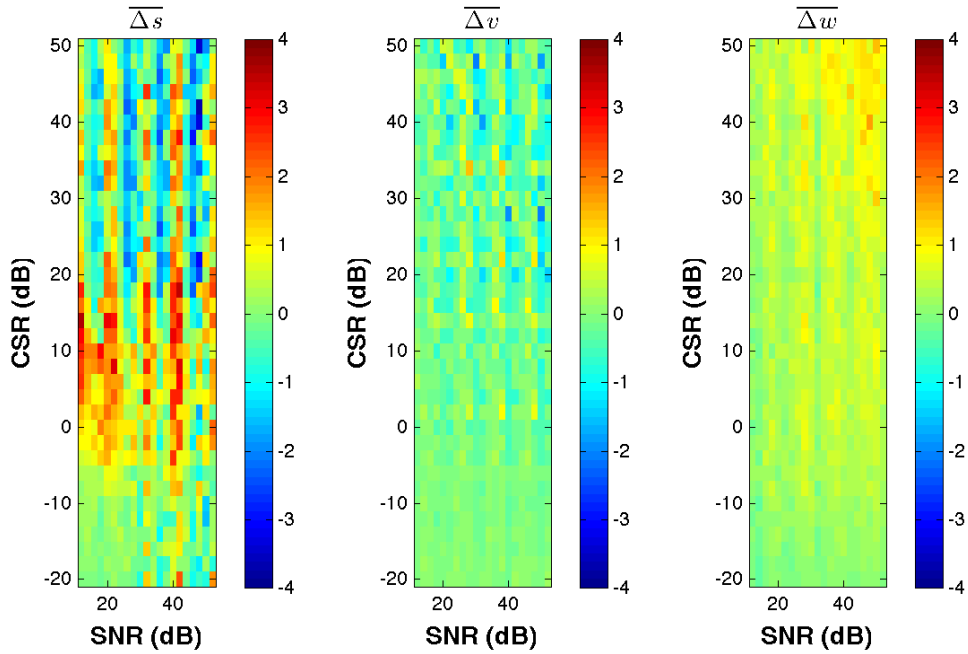

Figure 3.22: Performance of the RDR algorithm for stratiform precipitation weather signals with velocity magnitude between 1 $\mathrm{m\,s^{-1}}$ and 5 $\mathrm{m\,s^{-1}}$.

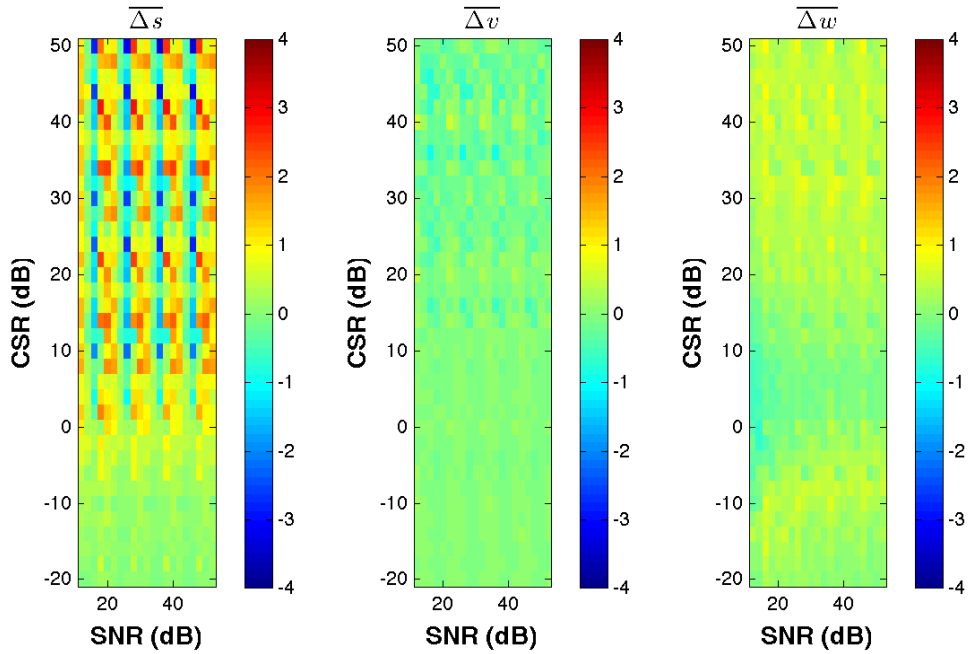

Figure 3.23: Same as Figure 3.22 except for weather signals with velocity magnitude between 5 $\mathrm{m\,s^{-1}}$ and 15 $\mathrm{m\,s^{-1}}$.

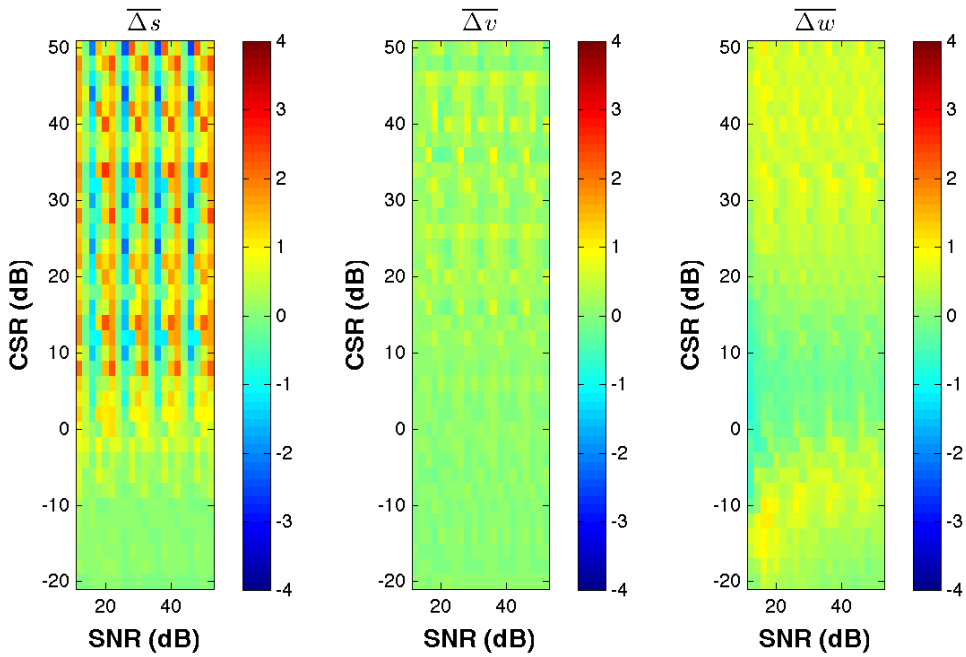

Figure 3.24: Same as Figure 3.22 except for weather signals with velocity magnitude larger than 15 $\mathrm{m\,s^{-1}}$.

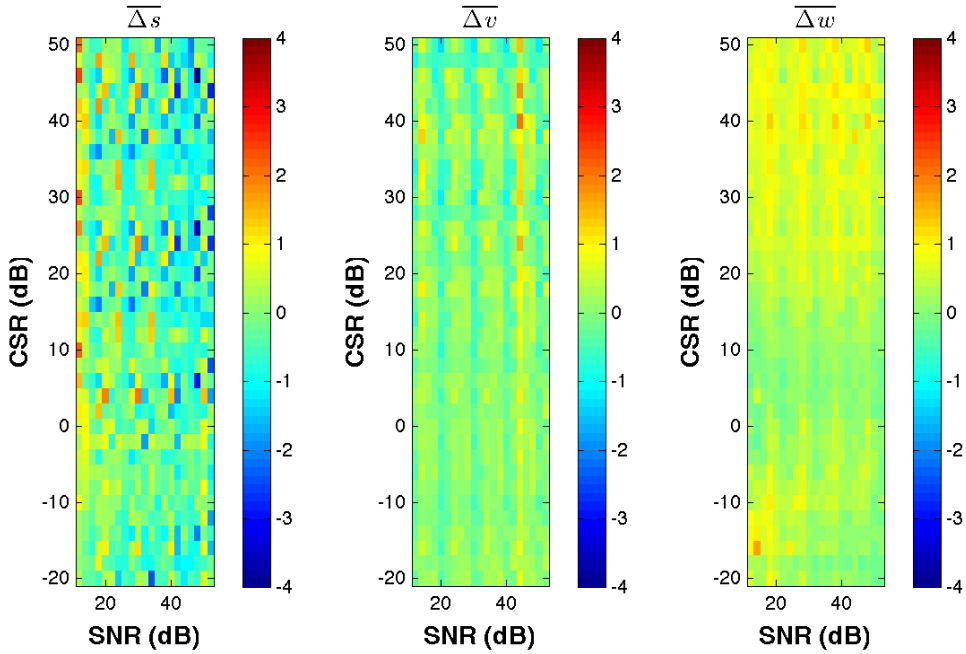

Figure 3.25: Performance of the RDR algorithm for convective storm weather signals with spectrum width less than 2 $\mathrm{m\,s^{-1}}$.

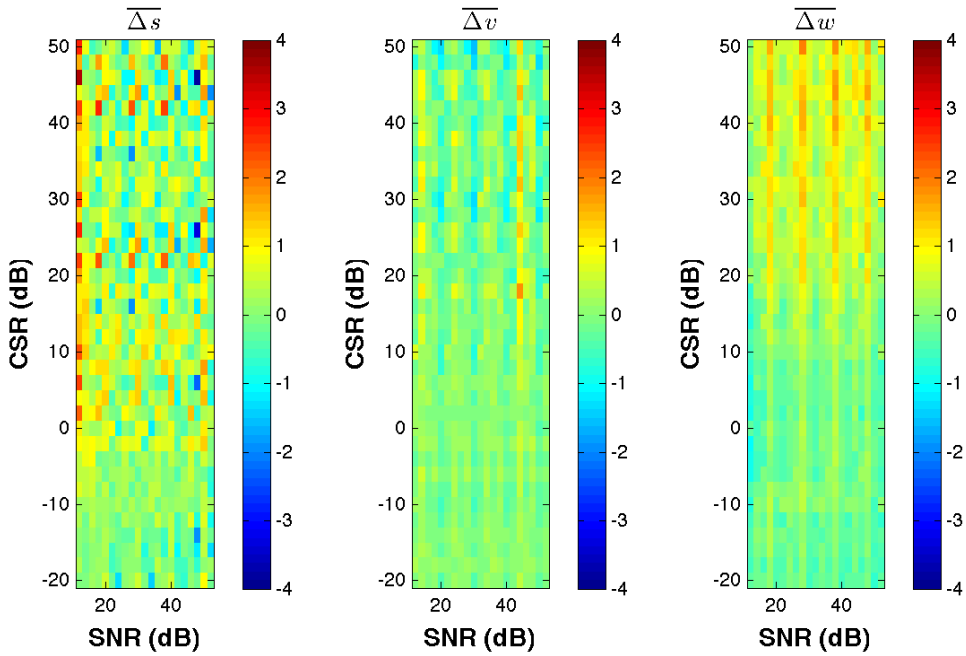

Figure 3.26: Same as Figure 3.25 except for weather signals with spectrum width between 2 $\mathrm{m\,s^{-1}}$ and 4 $\mathrm{m\,s^{-1}}$.

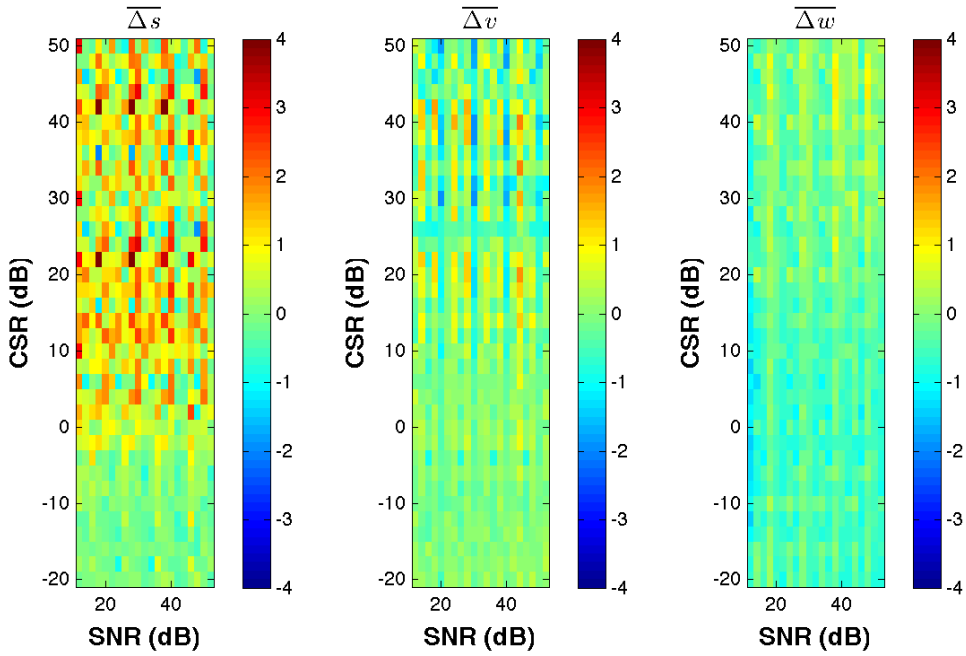

Figure 3.27: Same as Figure 3.25 except for weather signals with spectrum width between 4 $\mathrm{m\,s^{-1}}$ and 6 $\mathrm{m\,s^{-1}}$.

shows that the number of range gates with spectrum width greater than 4 $\mathrm{m\,s^{-1}}$ less than half of the number of range gates with spectrum width between 2 $\mathrm{m\,s^{-1}}$ and 4 $\mathrm{m\,s^{-1}}$. Also, the range gates with spectrum width larger than 4 $\mathrm{m\,s^{-1}}$ mostly come from simulations with $\overline{w} = 4\ \mathrm{m\,s^{-1}}$and they all have spectrum width greater than the average spectrum width for that range profile, which implies they are from the same range gates in different simulated profiles. Since the low-order polynomial fit was used to determine the weather signal power estimate for high CSR cases, contaminations at same location would result in similar fits with similar delta biases since the weather signal power used to generate the fit are different by a constant, especially for stratiform precipitation. The high mean delta biases are the results of not having positive and negative delta canceling out.

Through simulations, the RDR algorithm is proven to be capable of reducing the biases introduced by WTC contamination for a wide range of SNR and CSR. However, as shown in Figure 3.22, weather signals with velocities near 0 $\mathrm{m\,s^{-1}}$ are not handled well by the RDR algorithm. Similarly, when the algorithm has to rely on the fit to produce the weather signal power estimates, large biases could occur on a gate to gate basis. Also, the CSR estimators have large variances and can only operate well for limited CSR ranges. These limitations of the RDR algorithm need to be investigated further before an operational algorithm can be implemented.

3.2.3 RDR Algorithm on Non-Contaminated Gates

One key requirement of the RDR algorithm discussed in Section 2.4.1 in the approximate knowledge of the contaminated gates. It was argued that a conservative estimation of contaminated gates based on the known locations of the wind turbines can also be used to satisfy the requirement. Figure 3.28 and 3.29 show the delta biases of the spectral moment estimates introduced by the RDR algorithm for non-contaminated gates if they was treated as contaminated by the RDR algorithm. For stratiform precipitation, the delta bias of signal power caused by the RDR algorithm for non-contaminated gates are within ± 0.5 dB and the delta bias of velocity and spectrum width are less than $\pm 0.5\ \mathrm{m\,s^{-1}}$ for SNR range from 12 dB to 52 dB. For convective storm, the delta biases of signal power is within ± 1 dB and the delta biases of velocity and spectrum width are less than $\pm 0.5\ \mathrm{m\,s^{-1}}$. Figure 3.28 and 3.29 shows that the delta biases of the spectral moment estimates caused by the RDR algorithm are small for non-contaminated gates, and they justify the use of a conservative estimation of contaminated gates based on the known locations of the wind turbines as the approximate knowledge of the contaminated gates.

3.3 Performance on Real Radar Data

The RDR algorithm performed well in mitigating the WTC contamination in the simulations, but it must be tested on real data as well. The data set selected to test the RDR algorithm was collected by the KOUN research radar located in Norman, OK, on June 29, 2011, at 11:29:57 UTC at an elevation of 0.5 degree. The PPI plots

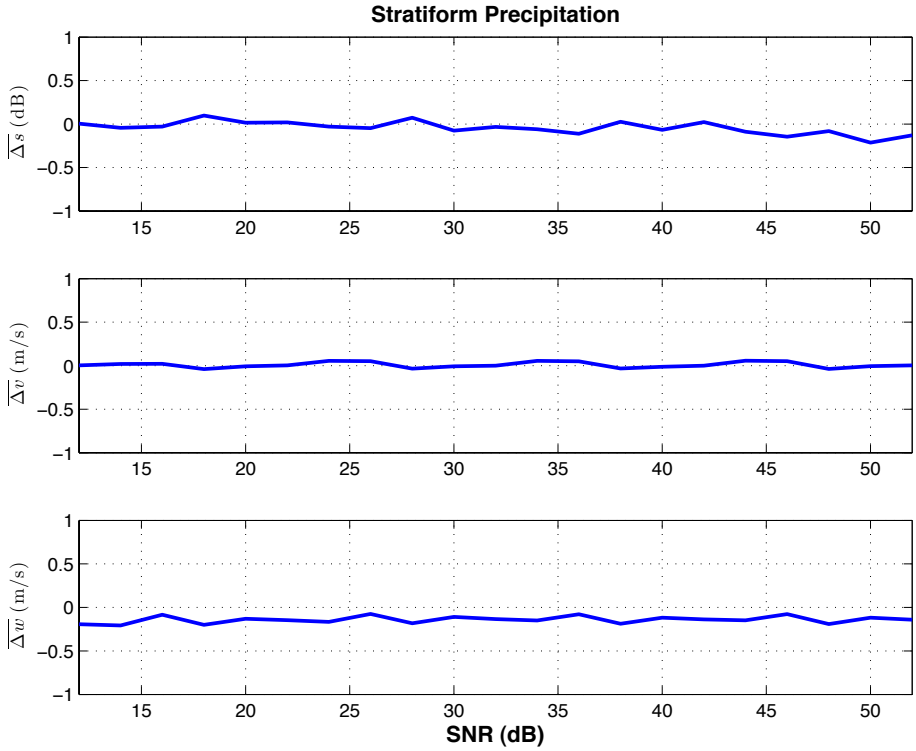

Figure 3.28: Mean delta biases of the three spectral moment estimates of range gates that were non-contaminated but were treated as contaminated by the RDR algorithm for stratiform precipitation. The x-axis is the SNR of the weather signal.

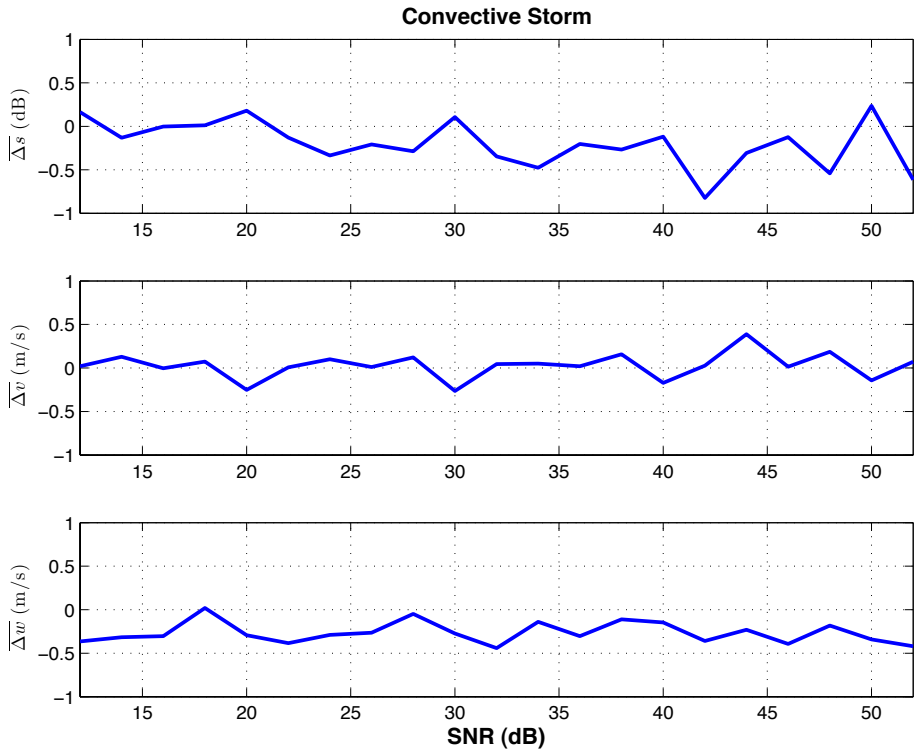

Figure 3.29: Same as Figure 3.28 except for convective storm.

of the spectral moment estimates before and after applying the RDR algorithm are shown in Figure 3.30

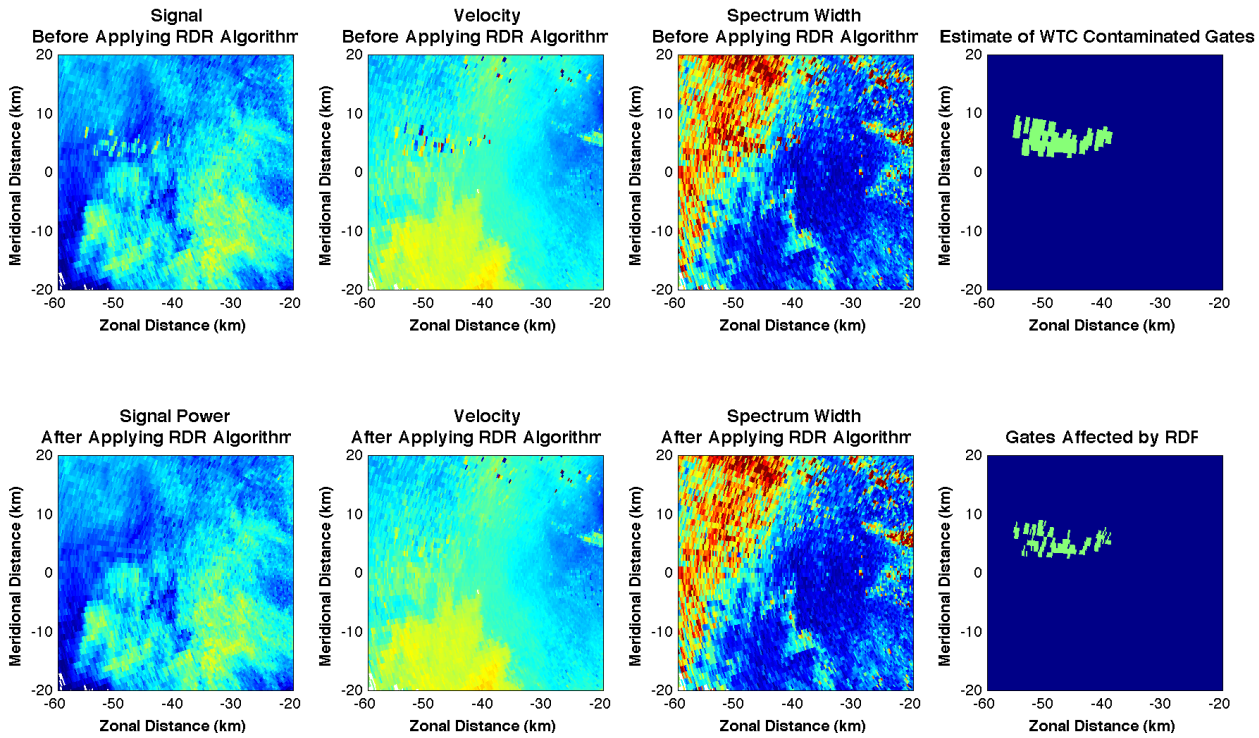

Figure 3.30: PPI plots of the spectral moment estimates before and after applying the RDR algorithm along with the estimated contaminated gates and the gates actually affected by the RDR algorithm. SNR censoring was done on the PPI plots with 2 dB threshold for signal power and 3.5 dB threshold for velocity and spectrum width.

The top right plot in Figure 3.30 shows the known contaminated gates locations used by the RDR algorithm. It was generated by dilating a WTC clutter map with a three by three square structuring element. The initial WTC clutter map was generated by measuring the distance and azimuth angle of each wind turbine to the radar using GPS location information from the FAA. Since the uncontaminated spectral moment estimates were unknown, the performance of the RDR algorithm can only be evaluated qualitatively. Before applying the RDR algorithm, the contaminated range gates have observable elevated power level, random velocities that are distinct from neighboring gates, and large spectrum width. After applying the RDR algorithm, the elevated power level are reduced and matches the power level of the neighboring gates. Similarly, the large velocity fluctuations in the contaminated gates are eliminated and the new velocity estimates matches the velocity estimates of the neighboring gates. The spectrum width estimates after are smaller than the original estimates after applying the RDR algorithm. It is unfortunate that the WTC contaminated gates are located in a region with low SNR so the improvements in the spectrum width estimates are not as clear as the improvements in signal power and velocity estimates. The bottom right plot of Figure 3.30 shows the range gates where the RDR algorithm produced different spectral moment estimates than the original estimates. Comparing the gates actually affected by the RDR algorithm to the approximate clutter map above shows that a conservatively estimated clutter map is a good way to approximate the knowledge of the contaminated gates since the RDR algorithm is capable of leaving miss identified gates alone.

The RDR algorithm could reduce the biases caused by WTC contamination in real observations, but several issues must be solved before it can be developed into an operational algorithm. First, the performance dependence on the number of samples in the time series need to be studied. In the simulations, the number of samples of each time series was set to 80, but there are often less samples available in real observations. Secondly, in the simulations and the real data, there were no range overlaid echos, which would need special handling in an operation algorithm. Finally, to satisfy the accuracy requirement of an operational algorithm, the variance of the delta biases after applying the RDR algorithm need to be reduced.

Chapter 4

Conclusions and Proposed Path Forward

Over the performance period of this project, several WTC mitigation schemes, based on advanced signal processing methods, have been explored. Adaptive beamforming, wavelet transformation, and other non-stationary signal processing techniques are a few examples. After this extensive review of the state-of-the-art, the most potential has been found in image processing methods based on mimicking the ability of humans to perceive continuity, or flow, in images. For the weather radar case, the atmosphere is a fluid governed by the viscosity and dynamics of the medium. As such, the desired weather signal must exhibit spatial continuity especially in the range-Doppler domain, as shown by several examples in this report. Of course, limitations exist for this assumption in high wind shear or heterogeneous precipitation events. Nevertheless, spatial continuity in the weather signal does exist on some scale, and it is this difference with the highly discontinuous WTC signal that is exploited in the proposed solution to the wind turbine clutter challenge.

In Chapter 2, the concept of the range-Doppler spectrum was explored. By simple examination of typical weather examples, it became readily clear that spatial continuity was an obvious discriminator between weather and WTC. An edge detection method was presented with the goal of automatically determining uncontaminated Fourier bins in the range-Doppler spectrum to be used for moment estimation. Some advantages, but even more disadvantages, for this method were discussed, which gave rise to the development of the proposed Range-Doppler Regression (RDR) algorithm. Assuming the locations of the turbines are known, the RDR algorithm uses the differences between WTC and weather signals in the range-Doppler spectrum with the goal of determining which Fourier bins to use for information extraction. Unlike the edge detection method, RDR more effectively uses the spatial continuity of the weather signal in range. Extensive optimization results of the RDR algorithm were presented in Chapter 3 using sophisticated simulation methods based on actual WTC data from the Dodge City, Kansas WSR-88D radar. Care was taken to create a comprehensive and realistic simulation framework in which to evaluate the proposed RDR method. After optimization of the governing parameters of the algorithm, a test case was performed on actual data from the KOUN WSR-88D radar in Norman, Oklahoma. Both the statistical analysis and the real-data case show that the RDR method has great potential for solving the WTC problem and for realtime implementation, given that the processing is conducted in range time. It should also be noted that performance on a phased array radar with no beam smearing effects would be greatly enhanced.

Although preliminary analyses show great promise for the RDR algorithm as an operational tool for WTC mitigation, a concept of operations has not yet been defined. A comprehensive analysis using a wider variety of real data cases is needed to fully quantify the performance of the technique in operational settings and justify its

real-time implementation. However, a real-time implementation has to balance performance improvements with existing computational resources. Thus, careful design work is crucial to fit the RDR algorithm into the existing digital-signal-processing pipeline. Another important consideration stems from the ongoing upgrade of the NEXRAD network to include dual-polarimetric capabilities. It is believed that the addition of polarimetric range-Doppler spectra will prove useful in improving the robustness of the algorithm. Preliminary analysis of data collected with NSSL's polarimetric X-band mobile radar revealed WTC signatures that could be exploited in a similar fashion as described in this report. However, much work is needed to validate these assessments.

For these reasons, we are recommending that the RDR algorithm be strongly considered for an aggressive implementation program.

Bibliography

Department of Energy, 2008: 20% Wind Energy by 2030. Report from the Energy Efficiency and Renewable Energy.

Doviak, R. J. and D. S. Zrnić, 1993: *Doppler Radar and Weather Observations*. Dover Publictions, Inc., 2nd edition.

Energy Information Administration, 2011: Renewable energy consumption and electricity preliminary statistics.

Gallardo-Hernando, B., J. Munoz-Ferreras, F. Perez-Martinez, and F. Aguado-Encabo, 2011: Wind turbine clutter observations and theoretical validation for meteorological radar applications. *Radar, Sonar Navigation, IET*, **5**, 111 –117.

Hood, K., S. Torres, and R. Palmer, 2010: Automatic detection of wind turbine clutter for weather radars. *Journal of Atmospheric and Oceanic Technology*, **27**, 1868–1880.

Isom, B. M., R. D. Palmer, G. S. Secrest, R. D. Rhoton, D. Saxion, T. L. Allmon, J. Reed, T. Crum, and R. Vogt, 2009: Detailed observations of wind turbine clutter with scanning weather radars. *Journal of Atmospheric and Oceanic Technology*, **26**, 894–910.

Merrit, D. A., 1995: A statistical averaging method for wind profiler doppler spectra. *Journal of Atmospheric and Oceanic Technology*, **12**, 985–995.

Morse, C. S., R. K. Goodrich, and L. B. Cornman, 2002: The nima method for improved moment estimation from doppler spectra. *Journal of Atmospheric and Oceanic Technology*, **19**, 274–295.

Perry, J. and A. Biss, 2007: Wind farm clutter mitigation in air surveillance radar. *Aerospace and Electronic Systems Magazine, IEEE*, **22**, 35 –40.

Tietjen, B. W., 2005: Assessment of Windmill Impact on Airfield Primary Surveillance Radars.

Vogt, R. J., J. Reed, T. Crum, J. T. Snow, R. Palmer, B. Isom, and D. W. Burgess, 2007: Impacts of wind farms on WSR-88D operations and policy considerations. *23rd Conference on IIPS*, San Antonio, TX, January 17.

Wilfong, T. L., S. A. Smith, and R. L. Creasy, 1993: High temporal resolution velocity estimates from a wind profiler. *Journal of Spacecraft and Rockets*, **30**, 348–354.

Zrnic, D., 1975: Simulation of weatherlike Doppler spectra and signals. *Journal of Applied Meteorology*, **14**, 619.